Landslides triggered by recent earthquakes in Italy

E. Ausilio
University of Calabria, Rende, Italy

F. Silvestri
University of Napoli Federico II, Napoli, Italy

G. Tropeano
University of Cagliari, Cagliari, Italy

P. Zimmaro
University of California, Los Angeles, USA

ABSTRACT

This report provides a detailed description of seismically-induced landslides and rockfalls occurred in Italy during the 2016 Central Italy earthquake sequence. Relevant ground motion characteristics for all mainshocks of the sequence are analyzed. The report also provides a quantitative overview of spatial and temporal characteristics of the landslides and rockfalls occurred during the earthquake sequence. This latter has been characterized by three mainshocks: (1) ***M****6.1 24 August, (2)* ***M****5.9 26 October, and (3)* ***M****6.5 30 October. A relevant fraction of landslides has been caused by the first* ***M****6.1 mainshock; however, both the following events, especially the third* ***M****6.5 earthquake, exacerbated the slope instability in many locations and triggered several new and more serious ground failures. The overwhelming majority of the instabilities induced by the sequence are rockfalls in fractured rocks. Details of three selected high-value case histories are described: (1) the Nera rockslide, (2) the Pescara del Tronto landslide, and (3) the Accumoli landslide. Rainfall data during 2016 are also shown and described for selected locations in the epicentral area.*

INTRODUCTION

Landslides have been considered as secondary effects induced by earthquakes. These local phenomena affect the interested areas and can greatly increase the human, social and economic impact of an earthquake. Recently, several studies have highlighted the importance of these secondary effects on damage and loss of human life (e.g. Bird and Bommer, 2004).

Italy is characterized by a very frequent seismic activity and high instability hazard. As a result, in recent years, numerous earthquakes were recorded in Italy, causing ground failure including landslides and rockfalls. Before 1783, historical accounts of the occurrence of earthquake-induced landslides were typically incomplete and vague (Keefer, 2002). The first scientific post-earthquake reconnaissance including systematic documentation of landslides induced by earthquakes was undertaken in the Calabria region (Southern Italy) following the 1783 Calabrian earthquake sequence. (Sarconi, 1784, quoted by Cotecchia et al., 1986).

In the last century, Ambraseys (1976) and Govi (1977) documented ground failures triggered by the 1976 Friuli (Northern Italy) earthquake sequence, when landslides were almost entirely rock falls. Instability phenomena associated with the 1980 Irpinia earthquake (Southern Italy) were characterized by delayed initiation or reactivation. Cotecchia and Del Prete (1984) and D’Elia et al. (1985) observed coherent slides and earth flows that began moving between a few hours to a few days after the mainshock. Such phenomena were associated with increased spring flow and pore-water pressures. This has determined an anomalous distribution of landslides where landslide were more numerous at greater distances from the epicenter. More recently, ground failures triggered by the 1997 Umbria-Marche (Central Italy) earthquake were mainly disrupted landslides. The areal distribution of landslides in Umbria-Marche was characterized by a large amount of slope instabilities in the area adjacent to the epicentral area, with a decreasing trend with distance (Bozzano et al., 1998; Esposito et al., 2000).

In the period between August 24, 2016 and January 20, 2017, a wide Central Italy area has undergone a seismic sequence with three major earthquake events. The first event, with moment magnitude **M**6.1, occurred on 24 August 2016, the second (**M**5.9) on 26 October, and the third (**M**6.5) on 30 October 2016. Each event was followed by numerous aftershocks.

All mainshocks were caused by normal faults part of the Mt. Vettore-Mt. Bove fault system. The 24 August event caused massive damages especially to the villages of Amatrice, Accumoli and Arquata del Tronto. In total, there were 299 fatalities, generally from collapses of unreinforced masonry dwellings. The October events caused significant new damage in the villages of Visso, Ussita and Norcia, although not producing fatalities, since the area had largely been evacuated.

Several landslides and rockfalls were triggered by the seismic sequence. Volume and occurrence area of landslides caused by the August mainshock were limited, despite the steep morphology of the region and the significant seasonal rainfall that had occurred in the week preceding the 24 August event. For the instabilities triggered by the 24 August event, this report focuses on the results (and subsequent analysis) of reconnaissance missions performed by the following agencies:

(1) the Geotechnical Extreme Event Reconnaissance (GEER, 2016 and 2017) association,
(2) the National Institute for Environmental Protection and Research (ISPRA, 2016),
(3) the Research Center for Prediction, Prevention and Monitoring of Geological Risks of Sapienza University (CERI, 2016),
(4) National Institute for Geophysics and Volcanology (INGV, 2016).

Information about landslide features triggered and/or exacerbated by the October events are mainly based on observations made by the GEER team and CERI. The authors of this report participated in the GEER reconnaissance mission and subsequent analysis. The GEER reconnaissance mission was conducted during two phases:

(1) following the 24 August event, from early September to early October 2016,
(2) following the October events, between the end of November and the beginning of December 2016.

For the 26 October event, limited field observations are described from the short time window between this event and the subsequent 30 October event and do not include detailed mapping. As a result, more emphasis is placed on features triggered by the 24 August event, and exacerbated and/or triggered by the October events (i.e. observed during the second reconnaissance trip following the 30 October event).

The large majority of the observed instability features are rockfalls in fractured rocks. Many rockfalls observed after the October events are likely due to breakage of joints likely weakened by the 24 August event. The report describes three major landslides, judged as high-value case histories:

- the south-western flank of the Nera River valley, located south-west of the village of Visso, where a large rockslide was induced by the **M**6.5 30 October 2016 earthquake;
- Pescara del Tronto, where the 2016 events induced significant failures on a soil/rock slope overlooking the SS4 motorway, connecting the west to the east coast of Central Italy;
- Accumoli, where slope failures occurred at the southern spur of the hill on top of which the village is built.

For the case histories of Pescara del Tronto and Accumoli, attention is given to the cumulative damage (or lack thereof) due to multiple events, as many shaken areas were inspected after both August and October events and therefore changes in damage level have been documented. In particular, this zone of Central Italy has been affected by several historical rockfalls related to earthquakes. Some previous studies (Antonini et al. 2002; Carro et al. 2003; Gigli et al. 2014) focused on rockfall hazard and risk assessment in the Umbria-Marche Apennines (Central Italy) after the 1997–1998 Umbria-Marche earthquake.

SEISMIC SOURCES AND GROUND MOTION CHARACTERIZATION

The Central Apennine chain can be seen as the backbone of the Italian peninsula. The whole region is characterized by an extensional tectonic activity. This regional extension is accommodated, in the inner Central Apennines by a series of normal faults striking northwest-southeast (NW-SE) and dipping southwest (SW). Seismological, geometric, and kinematic characteristics of main seismogenic sources of the area are summarized in GEER (2016, 2017) and Galadini et al. (2018).

This is a region with a long history of destructive earthquakes. The locations of faults have been well studied and the effects of past earthquakes on villages and towns in the region is well documented.

The 2016 Central Italy sequence occurred in a gap between two earlier earthquake events, the 1997 **M**6.1 Umbria-Marche earthquake to the north-west and the 2009 **M**6.1 L'Aquila earthquake to the south-east (Figure 1a).

Figure 1b shows main active fault segments in the epicentral area of the 2016 Central Italy earthquake sequence. The **M**6.1 24 August event is a peculiar two-fault event caused by the rupture of the southernmost section of the Mt. Vettore-Mt. Bove fault system (MVBF in Figure 1b) and of the northernmost section of the Laga Mts. fault system (Amatrice segment, AF in Figure 1b). The 26 and 30 October events were both caused by the rupture of the Mt. Vettore - Mt. Bove fault system. Table 1 shows parameters and locations of the mainshocks and three main aftershocks (after Galadini et al., 2018).

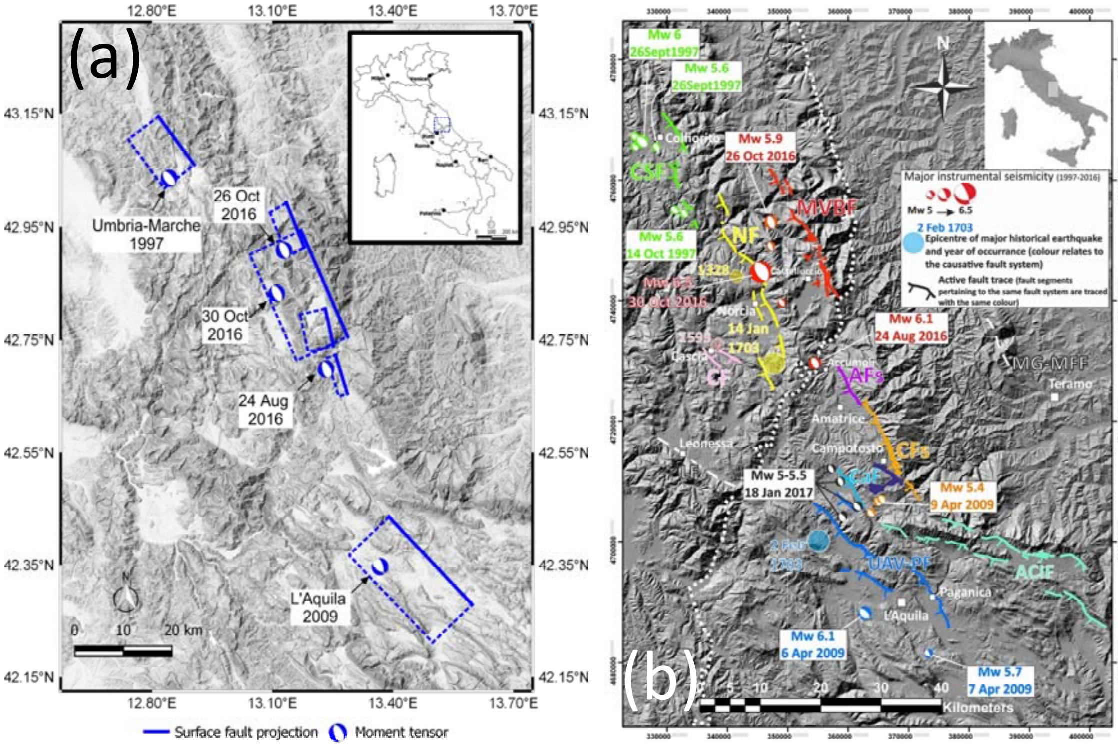

Figure 1: (a) Map of Central Italy showing moment tensors of major earthquakes since 1997. Finite fault models from Chiaraluce et al. (2004; 1997 Umbria-Marche event), Piatanesi and Cirella (2009; 2009 L'Aquila event), and Galadini et al. (2018; 24 August, 26, and 30 October 2016 events) are also shown. (from Lanzo et al. 2018); (b) Map showing active fault systems discussed in this chapter and locations of large seismic events in the region since 2009. Faults: Colfiorito-Sellano fault, CSF; Mt. Vettore-Mt. Bove fault, MVBF; Norcia fault, NF; Cascia fault, CF; Amatrice fault segment, AFs; Campotosto fault segment, CFs; Capitignano fault, CaF; Upper Aterno Valley-Paganica fault system, UAV-PF; Leonessa fault, LF; Monti Gemelli-Montagna dei Fiori fault, MGMFF. The Olevano-Antrodoco-Sibillini inactive thrust system is defined by the white dotted line. (from Galadini et al., 2018).

August 24, 2016 event

The mainshock occurred on the 24 August, 2016 at 01:36:32 (UTC) and was recorded by Italian National Seismic Networks (Rete Sismica Nazionale, RSN; www.gm.ingv.it/index.php/retesismica-nazionale/, last accessed 21 November, 2016) owned by the Italian Institute of Geophysics and Vulcanology (Istituto Nazionale di Geofisica e Vulcanologia, INGV). The 24 August 2016 mainshock event occurred along segments of normal fault systems trending NW-SE (strike ~165 deg) with a dip angle SW of ~45 deg. The strike of the fault from the moment tensor is generally consistent with the orientation of the Mt. Vettore fault to the north and the Laga Mountain fault to the south. The event occurred as a result of a multi-fault rupture between two fault systems, the Mt. Vettore-Mt. Bove and the Laga.

Table 1: Summary of the six selected main events that occurred in Central Italy between 24 August and 30 October 2016. Mainshocks are reported using bold-face fonts.

Date	Hour (UTC)	Latitude (N)	Longitude (E)	Depth (km)	**M**	Strike (deg)	Dip (deg)
08/24/2016	**01:36:32**	**42.70**	**13.23**	**8**	**6.1**	**168**	**41**
						Mt. Vettore-Mt. Bove	
						163	**52**
						Amatrice segment	
08/24/2016	02:33:28	42.79	13.15	8	5.3	134	56
08/26/2016	04:28:25	42.60	13.29	9	4.8	165	36
10/26/2016	17:10:36	42.88	13.13	9	5.4	160	38
10/26/2016	**19:18:05**	**42.92**	**13.13**	**8**	**5.9**	**158**	**43**
10/30/2016	**06:40:17**	**42.84**	**13.11**	**5**	**6.5**	**156**	**43**

Figure 2a shows the surface projection of the trimmed finite fault model for this event. The two fault systems involved in this rupture are: the Laga Mountains fault system (Amatrice segment), and the Mt. Vettore-Mt. Bove fault system. The number of aftershocks within 24-hour periods following 24 August mainshock were 121. Most of the aftershock epicenters are not within the surface projection of the hanging wall above the finite fault model, with many south and west of the rupture (Figure 2a).

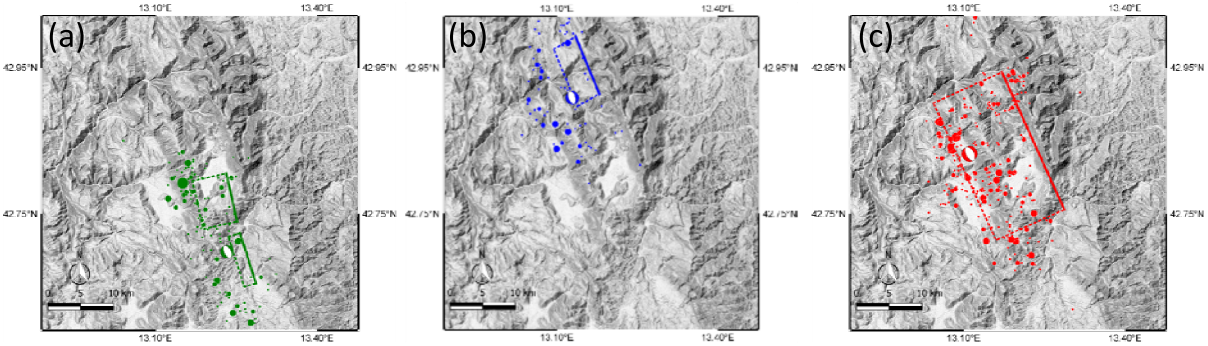

Figure 2: Trimmed finite fault model, moment tensor, and epicenter location for the (a) M6.1 24 August, (b) M5.9 26 October, and (c) 30 October event, along with aftershocks recorded within 24-hour periods following each mainshock (adapted from Galadini et al., 2018).

October 26 and 30, 2016 events

The hypocenter locations, slip directions, and surface rupture suggest that the 26 and 30 October events occurred on segments of the Mt. Vettore-Mt. Bove fault. As described in GEER (2016), this fault and the neighboring Laga Mts. fault to the south experienced rupture during the 24 August event. The 26 October event has an along-strike length of 8 km and down-dip width of 4 km. The 30 October event has an along-strike length of 21 km and down-dip width of 16 km. Figures 2b-c show epicenter location and surface fault projection for the 26 and 30 October event, respectively, along with aftershocks recorded within 24 hours from each mainshock.

Figure 3 shows the cumulative fault offset measurement (70 cm) on the lower or "western" fault trace (Lat = 42.812901, Long = 13.24626). A comprehensive overview of fault surface rupture observed during the 2016 Central Italy earthquake sequence is provided by GEER (2017) and Gori et al. (2018).

The number of aftershocks within the 24-hour period following each mainshock were 75 (26 October), and 258 (30 October). Aftershocks following these mainshocks have clear spatial patterns (Figure 2b-c). For the 26 October event, very few aftershocks actually occur within the surface projection of the rupture. The aftershocks pattern for the largest event (30 October) follows the expected pattern in which most epicenters occur within the surface projection of the rupture.

Figure 3: Incremental surface fault rupture on the western slope of Mt.Vettore-Mt. Bove fault.

Figure 4 shows the peak ground acceleration (PGA) spatial distribution in the epicentral area for all three mainshocks, along with the location of the selected case histories. All ground motion intensity measures presented in this paper are estimated using a kriging technique applied to within-event residuals (i.e. the difference between recorded and estimated ground motions using global ground motion models, for a specific earthquake event). In this approach, after calculating within-event residuals at all recording station sites, spatial distribution of a given intensity measure is estimated using the Jayaram and Baker (2009) global correlation model (i.e. a semi-variogram that describes the spatial variability of a given ground motion intensity measure throughout the area). The residuals are equal to zero at recording station sites. All source-to-site distance were calculated using trimmed finite fault models presented in Galadini et al. (2018). In this paper, within-event residuals are calculated using the average of the following Italy-adjusted global ground motion models: Boore et al. (2014), Campbell and Bozorgnia (2014), and Chiou and Youngs (2014). The Italy-specific regional adjustment adopted in these models is needed to capture a relatively steep ground motion attenuation with distance observed in Italian events (e.g. Stewart et al., 2012). Zimmaro and Stewart (2017) have recently illustrated the effectiveness of the adoption of global models with region-specific adjustments for ground motion characterization studies in Italy. Further details on the approach used to estimate the ground motion are provided in GEER (2017) and Zimmaro et al. (2018). An estimate of ground motion amplitudes in terms of PGA at the three selected mass-movements sites during the 24 August, 26 October, and 30 October 2016 mainshocks is provided in Table 2.

RAINFALL DATA BEFORE AND DURING THE EARTHQUAKE SEQUENCE

Three rain gauges are operated in the area affected by landslides/rockfalls: Endesa (Visso) and Ponte Tavola (Castelsantangelo Sul Nera) operated by Servizio Idrografico - Regione Marche, and Nerito-Crognaleto operated by Servizio Idrografico - Regione Abruzzo. Figure 5 shows the precipitation recordings in these gauges over the time-period of the event sequence (August to December 2016). The analysis of the rain gauges recording shows that non-significant precipitations occurred before the 24 August event. The largest amount of rain was recorded between August and October. However, as further discussed in the remainder of the report, none of the landslide features observed after the October events is related to rain effects.

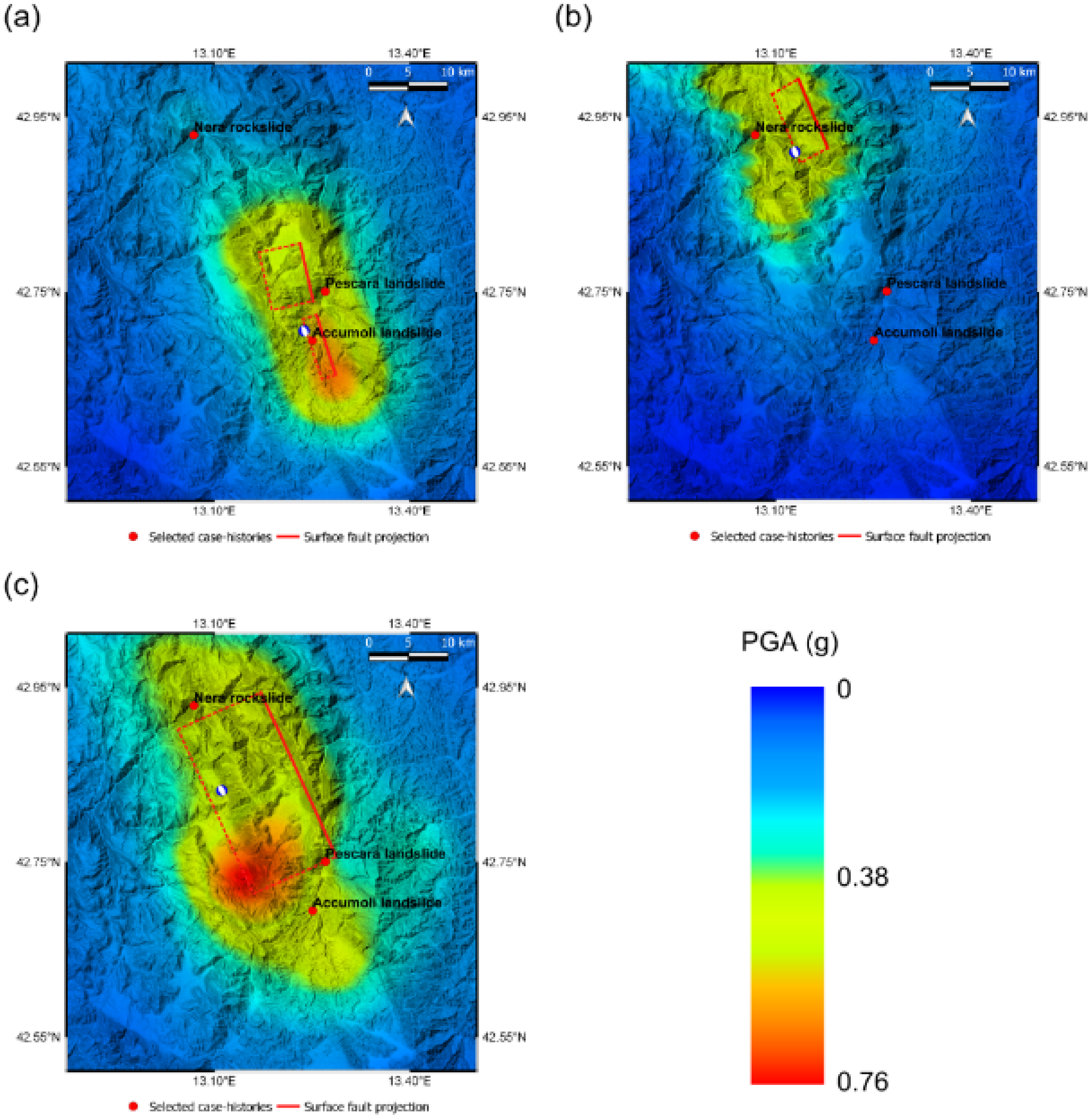

Figure 4: Spatial distribution of PGA (in units of g) estimated in the epicentral area for the (a) M6.1 24 August, (b) M5.9 26 October, and (c) M6.5 30 October events.

Table 2: PGA (in units of g) estimated at the selected mass-movements sites.

Lat.	Lon.	PGA (g)			Location Summary	Triggering event
		M6.1 24 August	**M5.9 26 October**	**M6.5 30 October**		
42.92900	13.06800	0.22	0.36	0.38	Nera Rockslide	M6.5, 10/30/2016
42.75057	13.27010	0.48	0.10	0.34	Pescara del Tronto	M6.1, 08/24/2016
42.69442	13.25029	0.55	0.07	0.40	Accumoli	M6.1, 08/24/2016

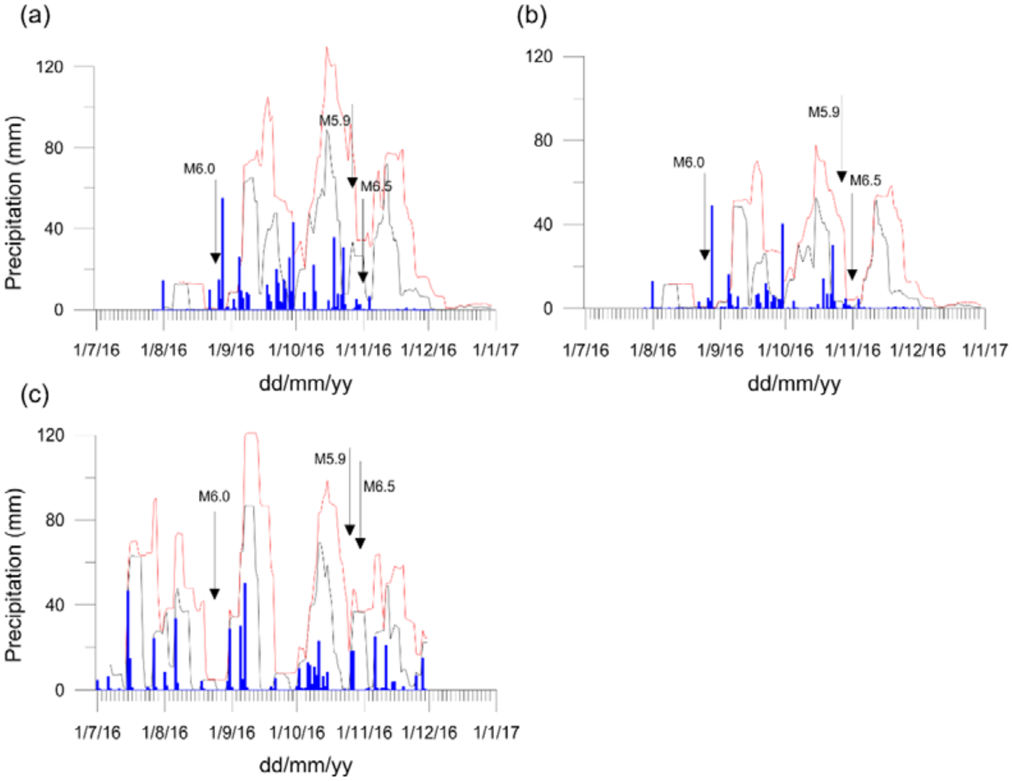

Figure 5: Daily rainfall (blue bars) and daily rainfall accumulated over one (black line) and two weeks (red line) recorded by (a) Visso, (b) Ponte Tavola (courtesy of Servizio Idrografico - Regione Marche), and (c) Nerito-Crognaleto (courtesy of Servizio Idrografico - Regione Abruzzo) rainfall gauges. (from GEER, 2016).

LANDSLIDE DATA

Many landslide sites are located in areas with rugged and/or steep terrain, heavy vegetation, and/or limited site access. As a result, for the GEER (2016, 2017) reports, Unmanned Aerial Vehicles (UAVs) have been extensively used to digitally image several significant landslides (Franke et al., 2018). Traditional on-site field reconnaissance investigations have also been conducted at several locations when road access was possible. Following Hungr et al. (2014), which updated the well-known Cruden and Varnes (1996) classification, landslides in the area can be classified as (Franke et al., 2018):

(1) rock fall and rock slides (rock planar- and rock wedge-slides involving the Miocene flysch and carbonatic units of the Umbria-Marche Succession),

(2) shallow translational and rotational soil slides in native slopes (e.g., cliffs, gulley banks, and steep natural slopes),

(3) shallow soil slides in anthropogenic slopes (e.g., steep roadway cuts and fills).

The information published in this report follow consistent description convention and categories. The landslides inventory was divided into the three main categories defined by Keefer (1984):

(1) Category I: falls and slides,

(2) Category II: coherent slides,

(3) Category III: lateral spreads or flow slides

No Category III features have been observed during the 2016 Central Italy earthquake sequence. When observed landslides do not fall into any of the mentioned standard categories or are not adequately described, they are labelled as "*other*" category. Landslide phenomena observed following the three main events of the seismic sequence are described below.

Landslides following the 24 August 2016 event

Several landslides have been observed following the 24 August mainshock. Figure 6 shows the mapped slope instabilities locations. Table 3 and Figure 7 summarize the percentage of landslides falling into each category and the different types of landslides for each category, following the 24 August event. Most of the observed phenomena fall in Category I and involve mainly small rock falls observed along roadways cuts throughout the earthquake zone.

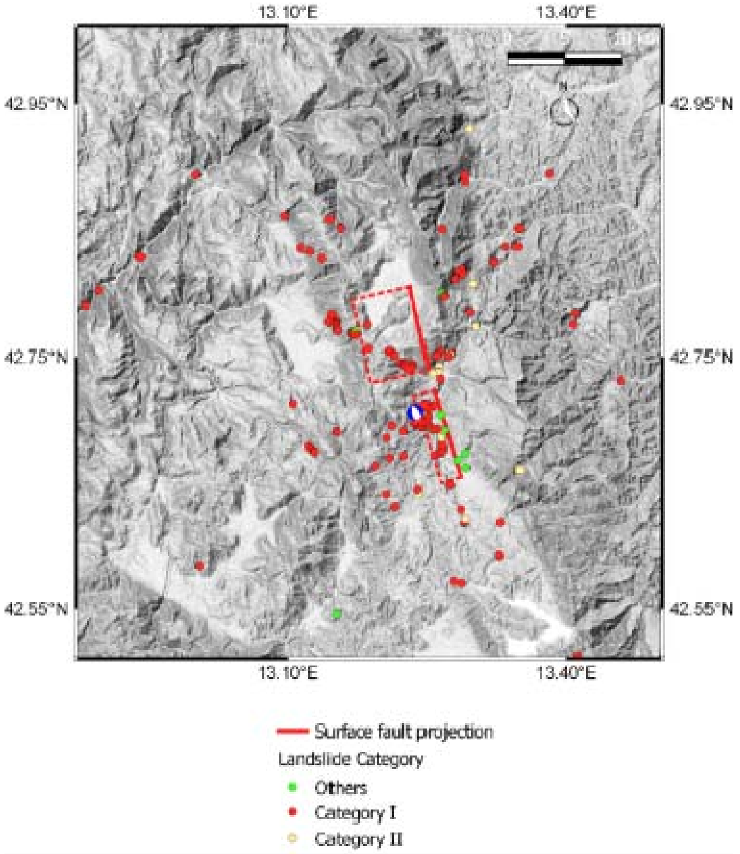

Figure 6: Observed landslides following the M6.1 24 August event.

Table 3: Categories of landslide occurred following the 24 August event.

Category I	Category II	Other
83.1%	9.6%	7.3%
Rock fall 95% Rock slide 5% (7/148)	Debris slide 71% Rock slide 29% (5/17)	

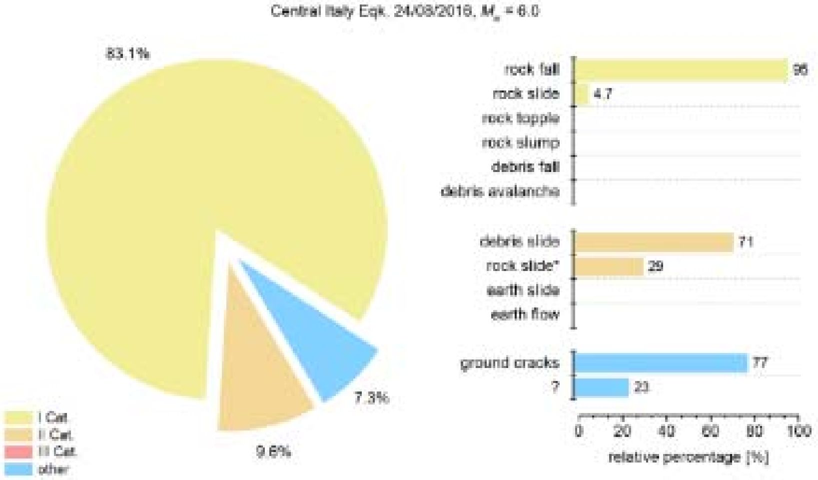

Figure 7: Distribution of recognized landslides after the 24 August event.

From a geological point of view, the area is characterized by Miocene flysch units and the Carbonatic units of the Umbria-Marche Succession. Flysch units (Laga formation) consist of alternating sandstone and marls layers, where sandstone is always the prevailing component. The flysch, similar to many other turbidite formations, presents variations in sandstone/marl ratio and layer thickness due to the distance from the source area in the depositional basin. Discontinuity spacing further varies depending on the distance from fault zones. Weathering of marl layers, though limited to extremely shallow depth, occurs soon after marls are exposed from highway cuts and excavations. This weathering is sufficient to undercut overlying sandstone slabs, which can break free when exposed to strong ground motions.

The most impressive rock fall features were observed in the area along state provincial routes SP64 (Tufo–Castelluccio) and SP477 (Castelluccio-Norcia). Almost all of the rockfalls occurred when isolated blocks of limestone detached from outcropping bedrock above the highway. Many of these blocks came to rest on the shoulder or pavement of the road, whereas other blocks maintained enough velocity to cross the road and continue descent downslope. An example of isolated blocks on highway SP477 is shown in Figure 8a-b. Figure 8c shows an image of the 3D model developed for the SP477 rockfall using UAV-based imagery (GEER, 2016). The data collected about Category II mainly concern rock slides in gentle slope (labelled as "rock slide") and other phenomena referred to as "debris slide". Many ground cracks were reported along road embankments and landfills, mainly behind retaining structures.

Figure 9 shows landslide data for the 24 August event compared with the empirical upper bound limits defined by Keefer (1985) in terms of Richter surface-wave magnitude (equal to 6 for the 24 August event) vs epicentral distance (Figure 9a) and Joyner and Boore distance (Figure 9b). Figure 9c shows the comparison between the envelope area affected by landslides and the upper bound proposed by Keefer (1984) and Rodriguez et al. (1999).

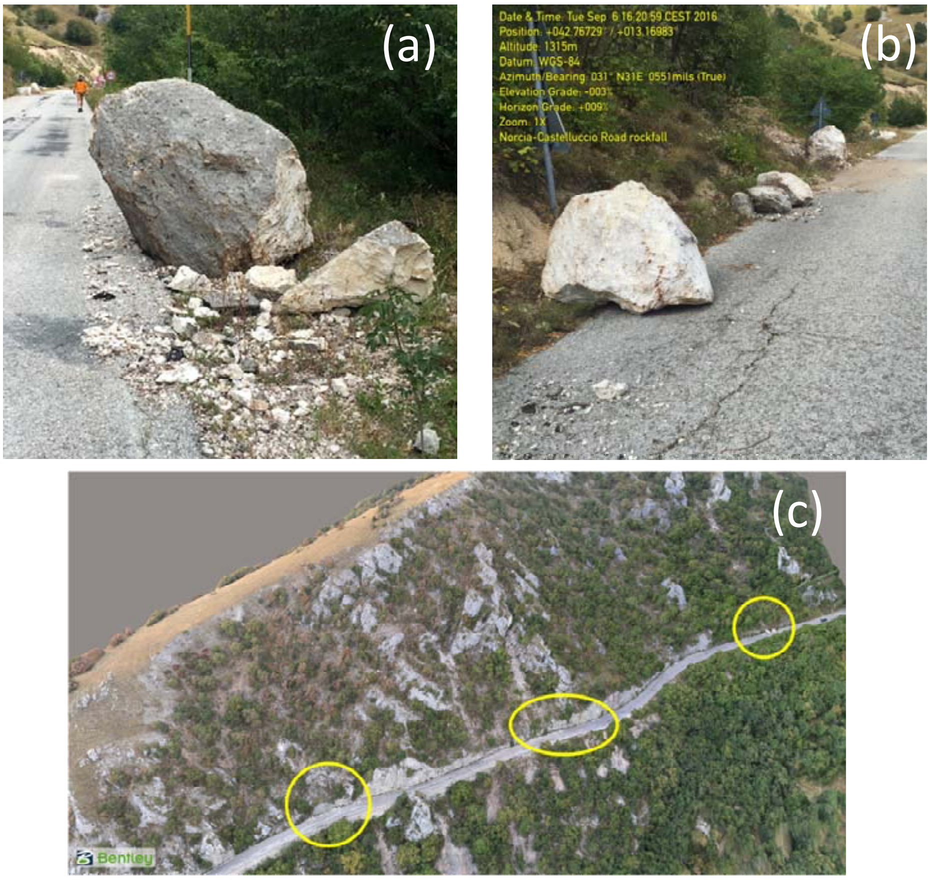

Figure 8. Example of rock fall on SP477 (42.76729 N 13.16983 E): (a) A large 2-m block of limestone crossed the road came to rest on the downslope side of the roadbed below a prominent outcrop of limestone (42.76729 N 13.16983 E); (b) Several blocks with size up to 3-4m; (c) 3D model of the area (from GEER, 2016).

The same information is reported in planar view in Figure 10. It shows the areal distribution of landslide sites compared with empirical upper-bound loci defined from Keefer (1985) for two source-to-site distance metrics: epicentral distance (Figure 10a), Joyner and Boore distance (Figure 10b).

The comparison with the empirical limits shows that the zone involved in the activation of Category I landslide is limited to an area with a radius of about 40 km around the epicenter (about half the distance limit indicated by Keefer (1985) for this kind of phenomena) with the majority being at 10 km or less from the surface ruptures. Comparing all mapped landslides with the Italian landslide inventory (Inventario dei Fenomeni Franosi in Italia, IFFI project, ISPRA – Dipartimento Difesa del Suolo Servizio Geologico d' Italia, available at: http://www.progettoiffi.isprambiente.it), new landslides are mostly in the near-field (<10km), while far-field landslides are present in the pre-existing landslide inventory (Pavlides et al., 2017).

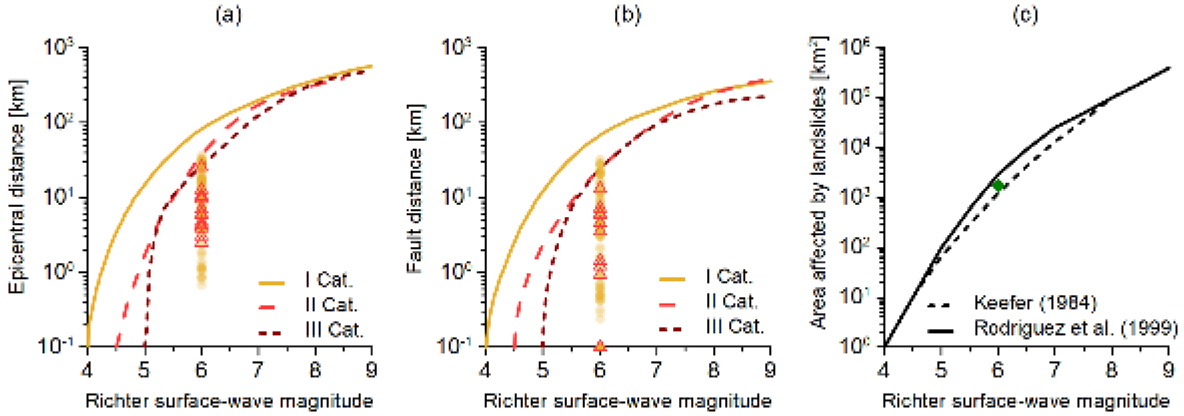

Figure 9: Comparison between source-to-site distances for landslides occurred following the 24 August event and the empirical upper-bound curves proposed by Keefer (1985) in terms of (a) epicentral distance and (b) Joyner and Boore distance; (c) comparison between the envelope area affected by landslides and the upper bound proposed by Keefer (1984) and Rodriguez et al. (1999).

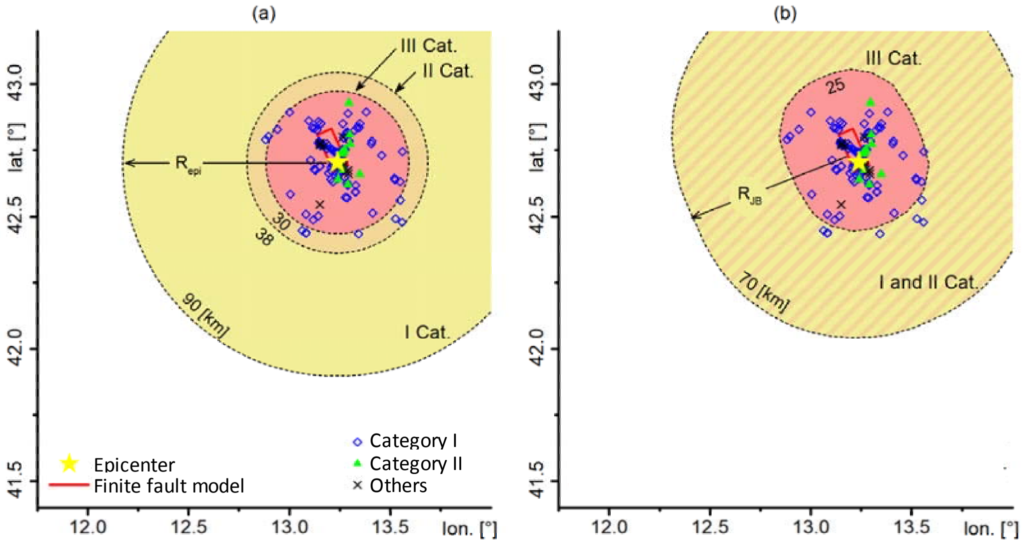

Figure 10: Areal distribution of landslide sites following the 24 August event compared with empirical upper-bound loci defined from Keefer (1985) for two source-to-site distance metrics: (a) epicentral distance, and (b) Joyner and Boore distance.

Landslides following the 26 and 30 October 2016 events

The October mainshocks triggered a larger number of landslide phenomena than the 24 August mainshock. These events, also exacerbated the amount of displacement caused by the 24 August in many areas. The types of instabilities are the same as those observed following the 24 August event. Figures 11a-b show all slope instabilities following the 26 and 30 October event, respectively. Tables 4-5 summarize the percentage of landslides falling into each category and the different types of landslides for each category following the October events. Figure 12 shows a graphical representation of the same information for the 30 October event. Similarly to what observed after the 24 August event, most of the observed phenomena fall in category I and involve rock falls.

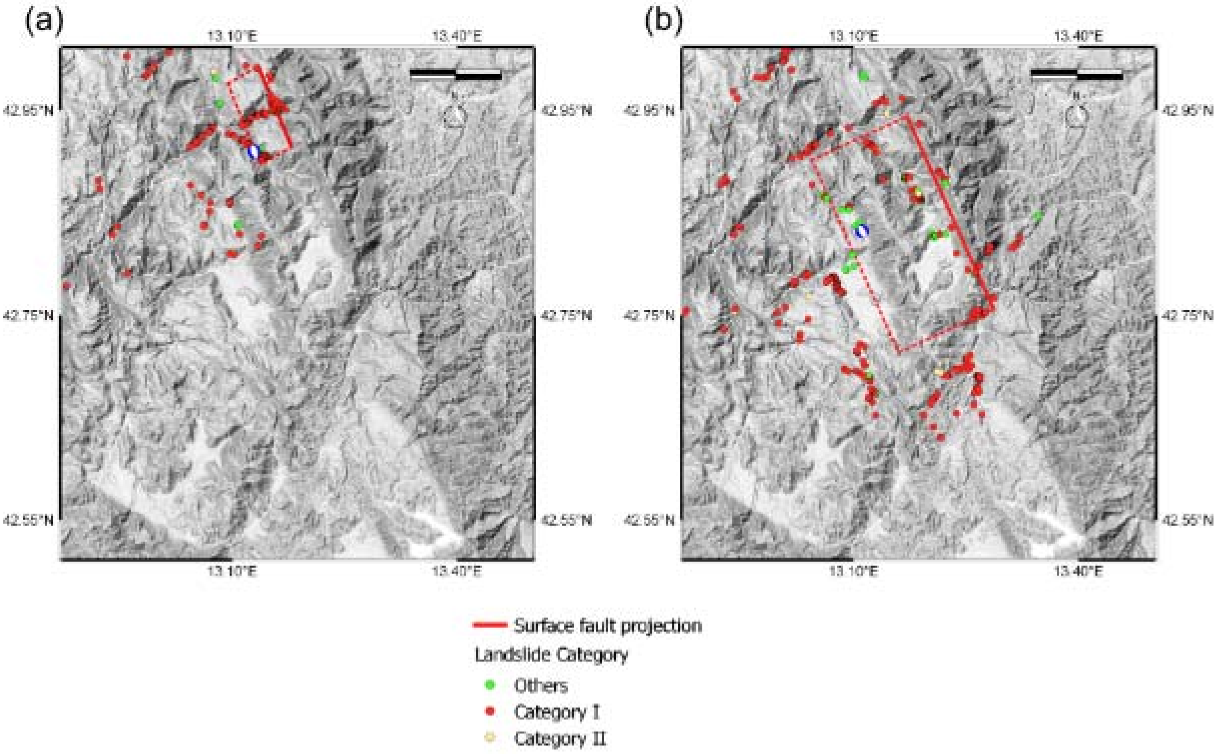

Figure 11: Observed landslides following the: (a) M5.9 26 October and (b) M6.5 30 October event.

Table 4: Categories of landslide occurred following the 26 October event.

Category I	Category II	Other
83%	10%	7%
Rock fall 95% Rock slide 5%	Debris slide 71% Rock slide 29%	

Table 5: Categories of landslide occurred following the 30 October event.

Category I	Category II	Other
83%	4%	13%
Rock fall 86% Rock slide 10% Rock topple >1% Rock slump 1% Debris fall 1% Debris avalanche >1%	Debris slide 66% Rock slide 13% Earth slide 13% Earth flow 8%	

Several rock falls observed following the October events are characterized by large volumes of involved material. The most impressive features observed following the 26 October event are probably the series of rockfalls in the area of Mt. Bove, 4 km east-southeast of Ussita. The northern flank of Mt. Bove is characterized by massive or coarsely bedded Jurassic limestones of the Calcare Massiccio Formation (MAS). At the top of the mountain the MAS formation is overlaid by limestones (Bugarone Formation) with more regular bedding (medium to thick beds). The Mt. Bove massif has been involved in intense quaternary and ancient tectonics which has produced faults trending in a strike range from ESE-WNW to N-S. The rock mass is characterized by closely spaced joints and persistent joints belonging to the major joint sets. Sever loosening of thick outer parts of the intensely fractured mountain flank could have favored the detachment of large irregular slices under seismic loading (GEER, 2017). Figure 13 shows a UAV-based image of a talus fields visible at the base of Mt. Bove. The same figure also highlights suspected source areas for these talus fields characterized by a lighter coloration of the freshly-exposed unweathered limestone (yellow circled in Figure 13).

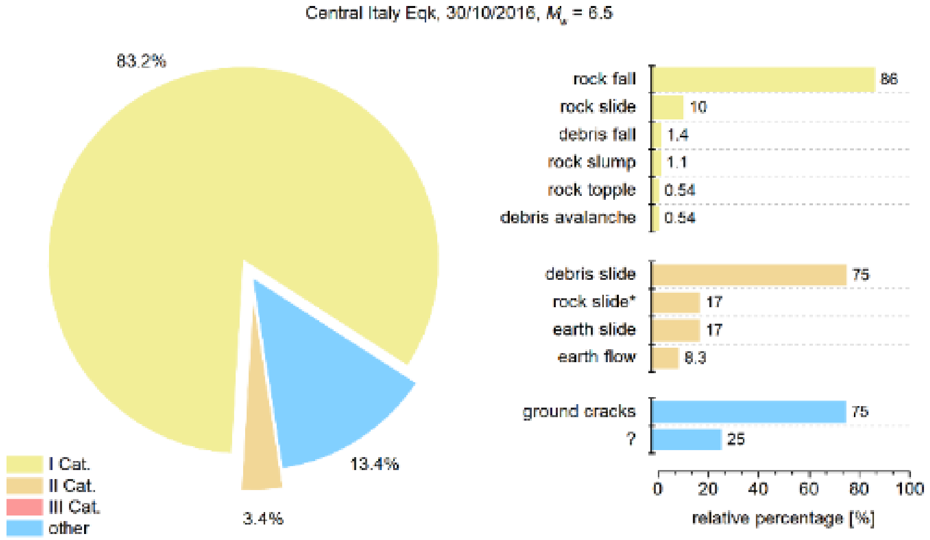

Figure 12: Distribution of recognized landslides after the 30 October 2016 earthquake.

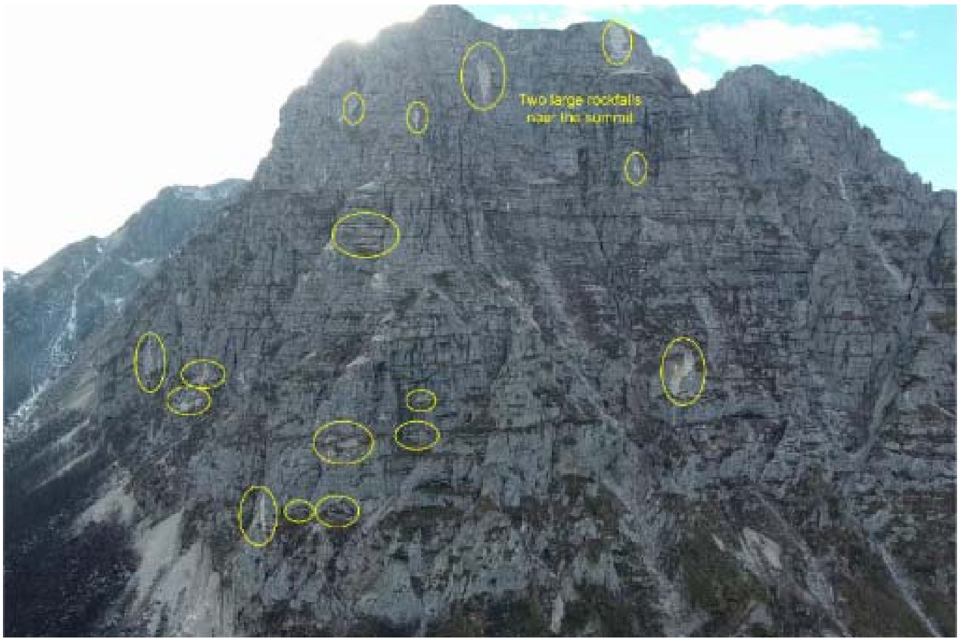

Figure 13: UAV image of Mt. Bove. Suspected rockfall sources are circled in yellow (from GEER, 2017).

Another interesting rockfall feature is that observed in the Valle di Panico. This instability phenomenon has been likely triggered by the 30 October event. However, this information is only inferred since prior information about it were not available at the time of reconnaissance (Lanzo et al., 2018). Mt. Bove represents the southern flank of the narrow valley called Valle di Panico. The northern flank of this valley is formed by a succession of limestone and marly units from Jurassic to Cretaceous in age. Two landslide locations along the mountain road that winds along the northern flank of Valle di Panico are present. The road is cut into thinly-bedded marly limestones (Scaglia Bianca Formation) whose bedding joints frequently have a clay/bituminous infilling. This structural/lithologic feature together an intense fracturing gives the rock mass quality a low quality. The source area of the rock fall at the second site is located in a marly-limestone unit featured by thicker layer. In this area the bedrock is extensively covered by slope debris some meter thick (GEER, 2017). The GEER reconnaissance team visited two main sites in the Valle di Panico area. The first site was a landslide in the soil slope through and beneath the road. Figure 14 shows an aerial photograph of this 55-60m wide landslide. The GEER team measured a vertical offset on the road pavement ranging between 10-70 cm, and an horizontal deformation ranging from 2-40 cm. The GEER team also created UAV-based 3D models of this landslides. As shown in Figure 15a, the eastern portion of the landslide headscarp shows distinct cracks and associated displacements. The western portion of the headscarp appears more gradual and shows pavement cracking (Figure 15b).

Figure 14: Aerial photograph of the Valle di Panico landslide (from GEER, 2017).

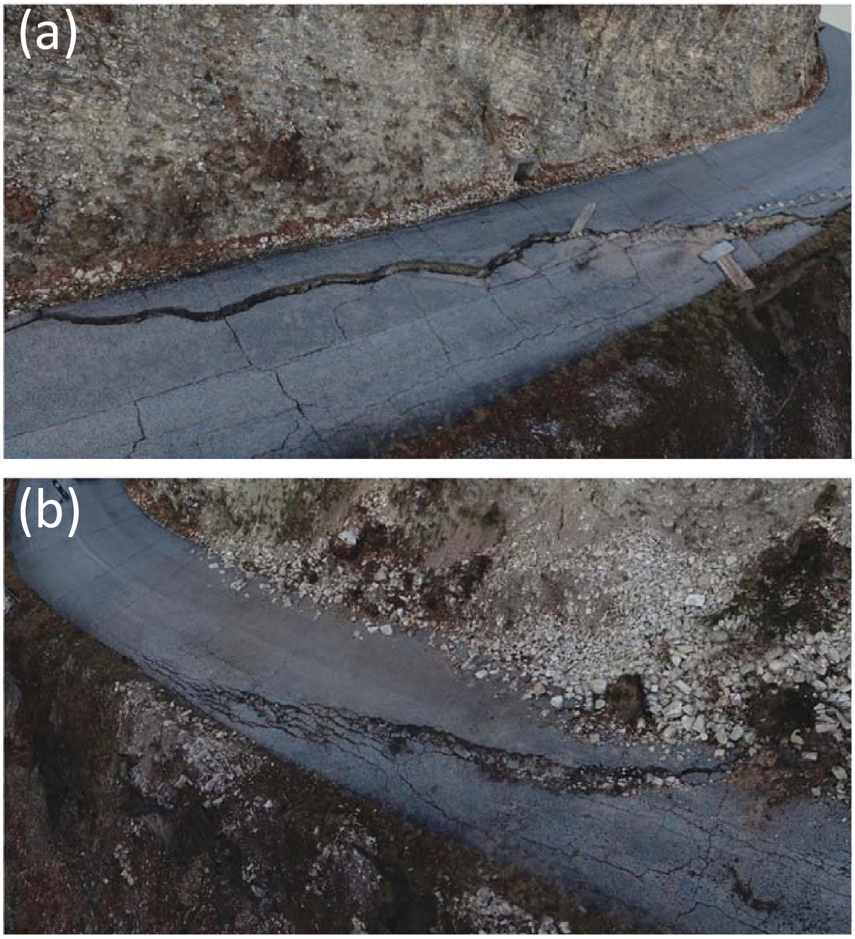

Figure 15: (a) 3D model of the eastern half of the Valle di Panico landslide headscarp; (b) 3D model of the western half of the landslide headscarp (adapted from GEER, 2017).

The second site in the Valle di Panico area is a 420m-long rockfall along a mountain road. Figure 16 shows a 3D model of the entire rockfall produced by the GEER team (GEER, 2017). The total change in elevation from the source of the boulder to the final resting place on the bottom of the valley is approximately 235 m. The sideslope of the valley rests at an angle of 34 degrees from the horizontal direction (1.5H:1V). Numerous boulder fragments ranging in diameter from gravel-size to over 3 m were observed and photographed along the entire rockfall length. The largest boulder measures 3m in diameter. The source boulder is 11.2 m in length and belongs to a formation of heavily weathered and fractured limestone located 91 m above the mountain road (Figure 17a). Much of the limestone boulder exploded into gravel-sized fragments in the first 90 m of the rockfall. The remaining parts of the boulder broke in larger fragments while tumbling to the bottom of the valley (GEER, 2017). At the bottom of the valley, over ten large boulder fragments ranging in diameter from 0.8-2.9 m were observed to rest at the valley floor just 13 m from what appeared to be a small pump or power house (Figure 17b). Information reported by the GEER team shows that none of the boulders appeared to damage this small structure (GEER, 2017).

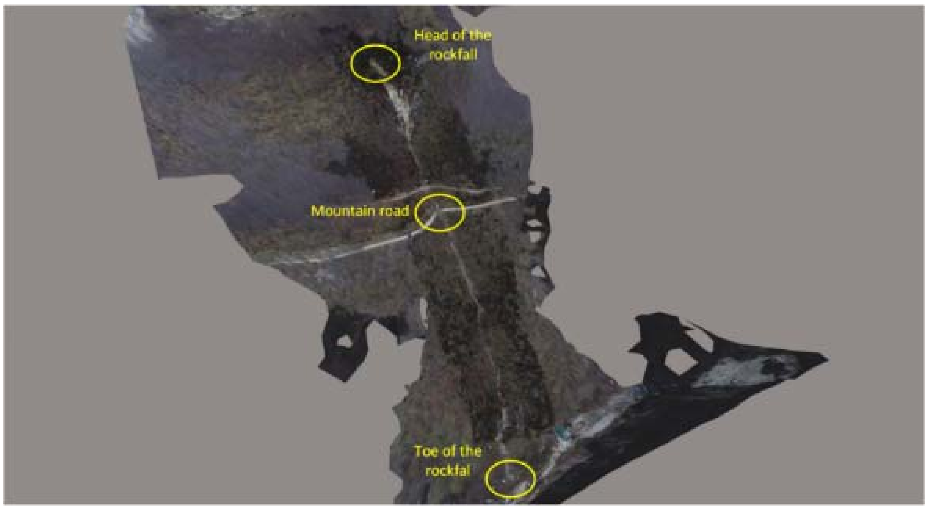

Figure 16: UAV-based 3D model of the Valle di Panico rockfall (from GEER, 2017).

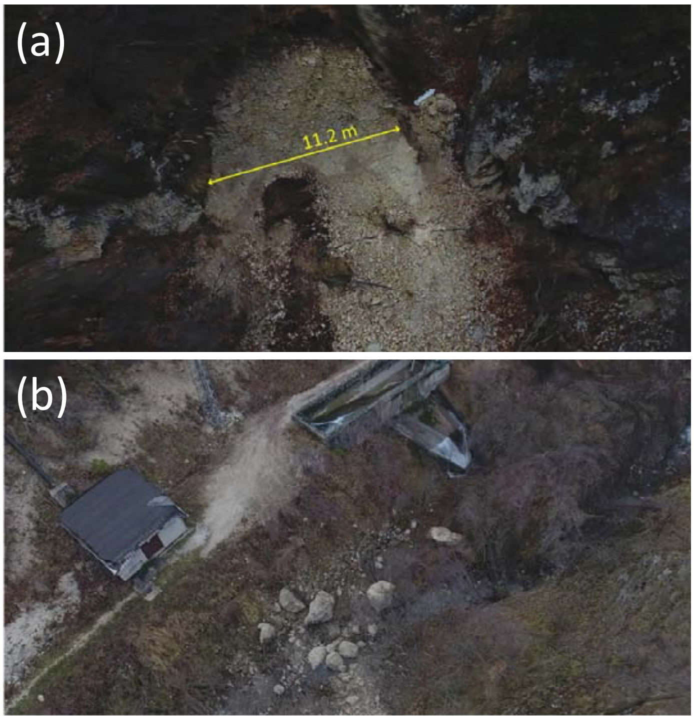

Figure 17: (a) 3D model of the source of the Valle di Panico rockfall, located 90 meters above the mountain road; (b) 3D model of the boulders and small power or pump house at the toe of the Valle di Panico rockfall (adapted from GEER, 2017).

Figure 18 shows landslide data for the 30 October event compared with the empirical upper bound limits defined by Keefer (1985) in terms of Richter surface-wave magnitude vs epicentral distance (Figure 18a) and Joyner and Boore distance (Figure 18b). Figure 18c shows the comparison between the envelope area affected by landslides and the upper bound proposed by Keefer (1984) and Rodriguez et al. (1999). The same information is reported in planar view in Figure 19. It shows the areal distribution of landslide sites compared with empirical upper-bound loci defined from Keefer (1985) for two source-to-site distance metrics: epicentral distance (Figure 19a), Joyner and Boore distance (Figure 19b). The comparison with the empirical limits shows that the zone involved in the activation of Category I landslide is limited to an area with a radius of about 40 km around the epicenter with the majority being at 10 km or less from the surface ruptures.

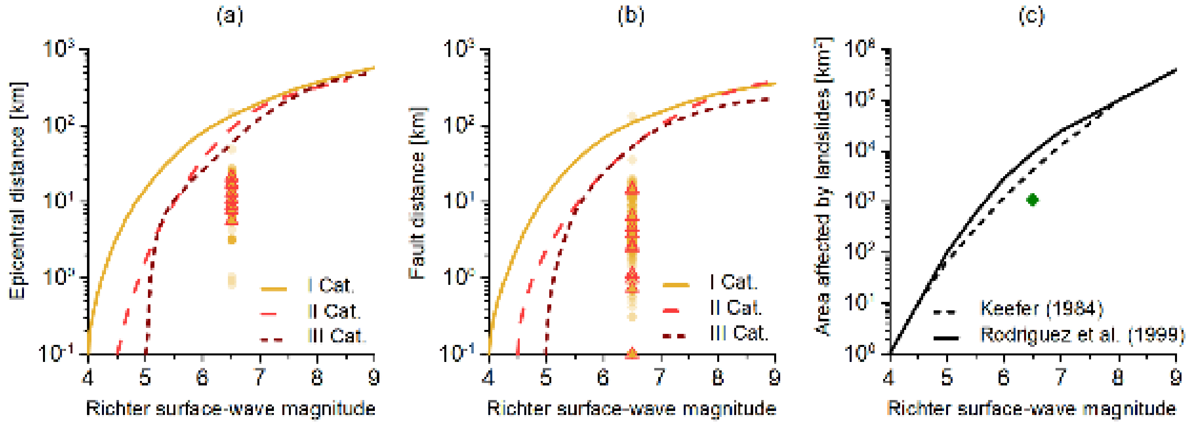

Figure 18: Comparison between source-to-site distances for landslides occurred following the 30 October event and the empirical upper-bound curves proposed by Keefer (1985) in terms of (a) epicentral distance and (b) Joyner and Boore distance; (c) comparison between the envelope area affected by landslides and the upper bound proposed by Keefer (1984) and Rodriguez et al. (1999).

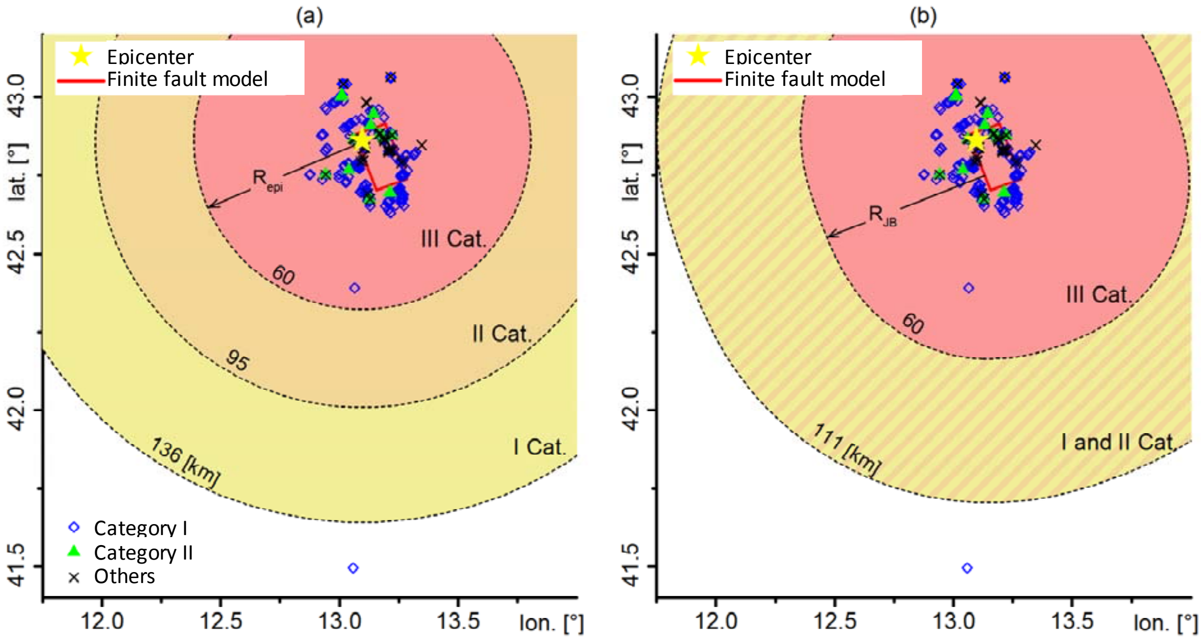

Figure 19: Areal distribution of landslide sites following the 30 October event compared with empirical upper-bound loci defined from Keefer (1985) for two source-to-site distance metrics: (a) epicentral distance, and (b) Joyner and Boore distance.

LANDSLIDE DETECTION DURING THE 2016 CENTRAL ITALY EARTHQUAKE SEQUENCE USING GEODETIC METHODS

Several geodetic methods use synthetic aperture radar (SAR) images to generate digital elevation models (DEM) for monitoring ground and structural deformations. These methods are typically based on differences in the phase of waves returning to a moving platform (e.g. aircrafts or satellites). SAR-based techniques are often utilized to identify deformation phenomena such as (1) earthquake-related surface deformations and ruptures (e.g. Jo et al., 2010), (2) volcanic eruptions (e.g. Jung et al., 2011; Lee et al., 2013), (3) subsidence (e.g. Choi et al., 2011; Zhang et al., 2012), and (4) massive landslides (e.g. Ausilio and Zimmaro, 2016). Such techniques have been also recently used to perform rapid detection and regional mapping of landslides following earthquakes (e.g. Rathje and Franke, 2016 following the 2004 Niigata-ken Chuetsu earthquake). It is worth noticing that satellite-based change detection methods usually underestimate the size of landslides (Rathje and Carr, 2010; Rathje and Franke, 2016). SAR-based methods are also used to produce rapid post-disaster deformation maps. This is one of the goals of the Advanced Rapid Imaging and Analysis (ARIA, 2016) project. The ARIA project team releases co-seismic interferograms and damage proxy maps (DPMs), following main natural disasters globally. The DPMs are produced by comparing interferometric SAR coherence maps from before and after an extreme event (e.g. Fielding et al., 2005; Yun et al., 2011). Yun et al. (2015) show that the extent of several observed earthquake-related instability phenomena following selected earthquakes were well captured by DPMs. Such maps have been also used to identify possible landslide and rockfall locations following the 2016 Central Italy earthquake sequence as shown in Figure 20 showing cluster of coherence changes in DPMs versus detected landslide features following the 21 August event (GEER, 2016 and Franke et al., 2018). Also Polcari et al. (2018) used SAR data to detect instabilities in the epicentral area of the 2016 Central Italy sequence, focusing on mountainous areas.

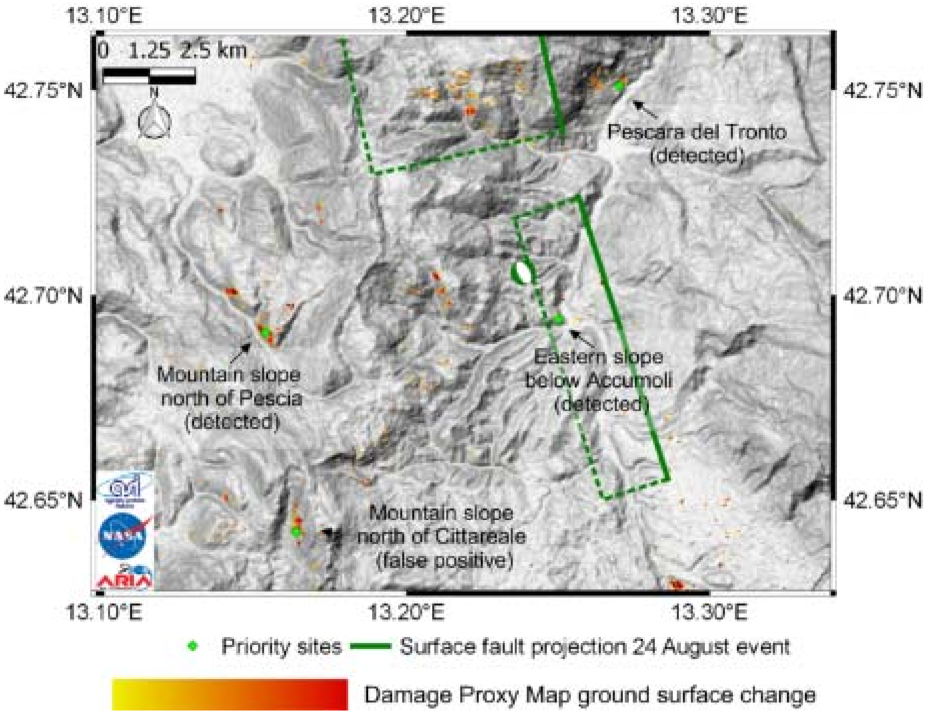

Figure 20: Epicentral area of the M6.1 August 24 earthquake along with damage proxy maps of the area produced by the ARIA project and detected landslide features (from Franke et al., 2018).

One of the instabilities detected by Franke et al. (2018) following the 24 August event is the Pescia rockfall. Figure 21 shows the UAV-based 3D models of the Pescia rockfall. At this location, the GEER team produced multi-epoch 3D models showing that after the detection of rockfalls following the 24 August event, additional boulders fell as a result of the 30 October event. The rock face reported in Figure 21 is approximately 90 m wide and 60 m high. The rock material that composes the face is a combination of limestone, argillaceous limestone, and Marlstone. Boulder sizes reach 2.5m. Next to this location, the GEER team detected additional rockfalls produced by the 30 October event, not present after the 24 August event. Figure 22 shows a 3D model of these features.

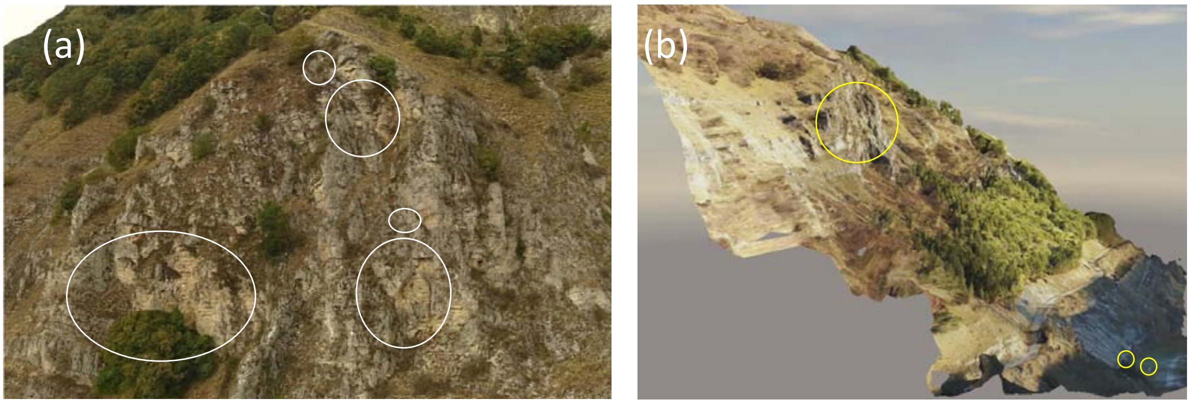

Figure 21: UAV-based 3D models of the Pescia rockfall following the (a) 24 August and (b) 30 October event (adapted from GEER, 2016 and 2017).

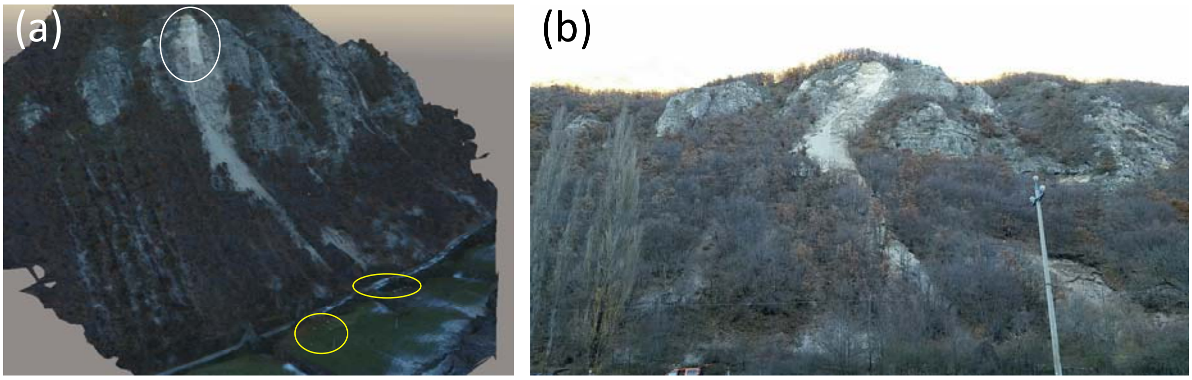

Figure 22: (a) UAV-based 3D models of additional rockfall feaures observed in the area of Pescia following the 30 October event; (b) source area of the rockfalls with runout damage.

RELEVANT CASE HISTORIES

This section focuses on three major landslide features, judged as high-value case-histories:

1. the south-western flank of the Nera River valley, located south-west of the village of Visso, where a large rockslide was induced by the **M**6.5 30 October 2016 earthquake known as Nera rockslide or Mount Sasso Pizzuto Rock Fall;
2. Pescara del Tronto, where the 2016 events induced significant cumulated damage on a soil/rock slope overlooking the SS4 motorway, connecting the west to the east coast of Central Italy;
3. Accumoli, where slope failures occurred at the southern spur of the hill on top of which the village is built.

GEER reports (2016 and 2017) show that incremental structural damage accumulation was particularly intense in Pescara del Tronto and Accumoli. Damage accumulation at these and other locations is due to the cycles of mainshock-aftershock sequences observed in the area between August and October 2016. Additional information about these selected case-histories are presented by Lanzo et al. (2018). Figure 23 shows the location of these case-histories along with epicenters of the three mainshocks of the sequence.

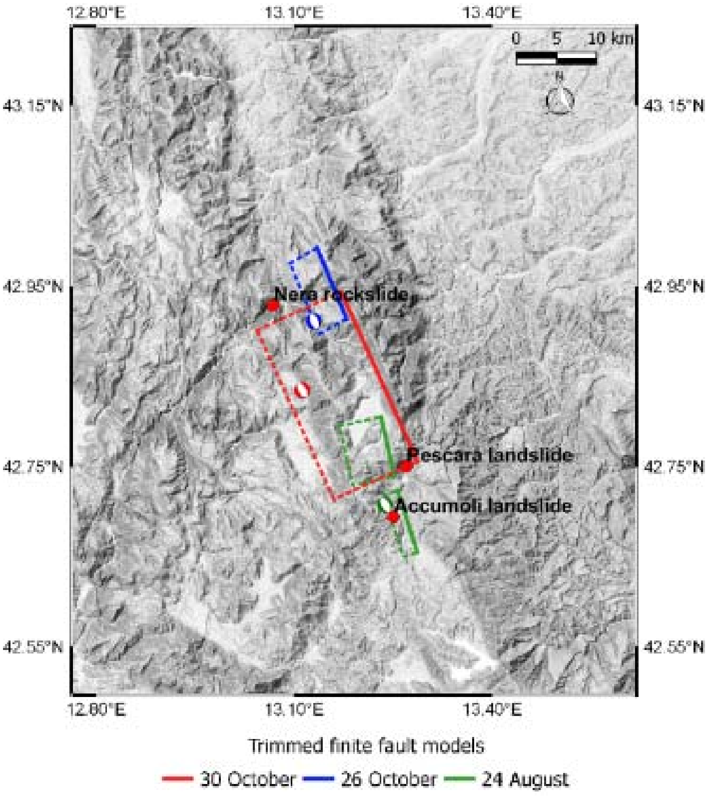

Figure 23: Location of selected relevant case-histories.

Nera rockslide or Mount Sasso Pizzuto rock fall

The Nera River Valley is huge canyon formed by the erosion of the Nera river, a tributary of the Tiber River, on limestone formations between the Umbria and Marche regional border (Figure 24).

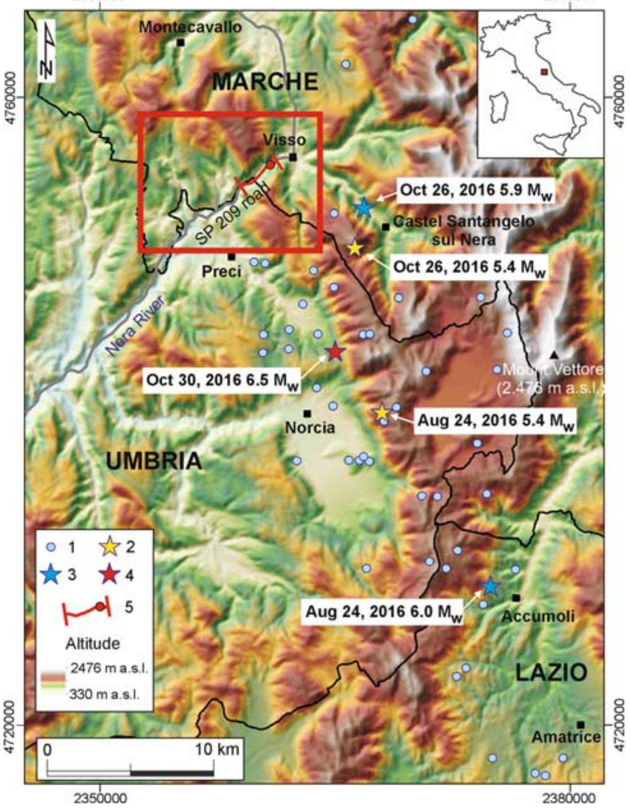

Figure 24: Location of the Nera river area between the Umbria and Marche regional border (from Romeo et al., 2017).

In some stretches the regional road (SP 209) rans along the Nera river. The Italian landslide inventory (Inventario dei movimenti franosi in Italia, IFFI project, ISPRA Dipartimento Difesa del Suolo Servizio Geologico d'Italia) classifies this area as subjected to rock falls and slumps. The Nera river valley area is characterized by sedimentary rocks of the carbonate Umbria-Marche stratigraphic sequence, an early Jurassic to Eocene age formation. The geology of the area (Romeo et al. 2017) is characterized by the outcropping of the Umbria Marche sequence from the Calcare Massiccio (a massive platform limestone) to Scaglia Variegata-Cinerea (marly-calcareous rocks). The Maiolica Formation (stratified pelagic limestone) is present in the left bank of Nera river. In some parts, the formations are pervasively folded (crumpled) and intensely fractured (Romeo et al., 2017).
Several rockfalls and diffuse instabilities occurred along this valley during the 2016 Central Italy earthquake sequence. Very few and small landslides were triggered by the 24 August event, while sever rock falls occurred following the October 2016 events. Boulders with a volume ranging from a dozen of cubic centimeters to a few of cubic meters, have been observed on the shoulders and/or across the road. Figure 25 shows cases in which the installed rockfall protection measures are passed over, severely damaged or destroyed. These passive protection measures (i.e. rockfall nets, dynamic rockfall barriers, rigid barriers or catch fences) were built along the SP 209 stretch after the 1997 Umbria Marche earthquake sequence which triggered about 200 rockfalls of various sizes along the Nera River Valley, and damaged man-made infrastructures such as roads, bridges and tunnels (Carro et al. 2003; Gigli et al. 2014).

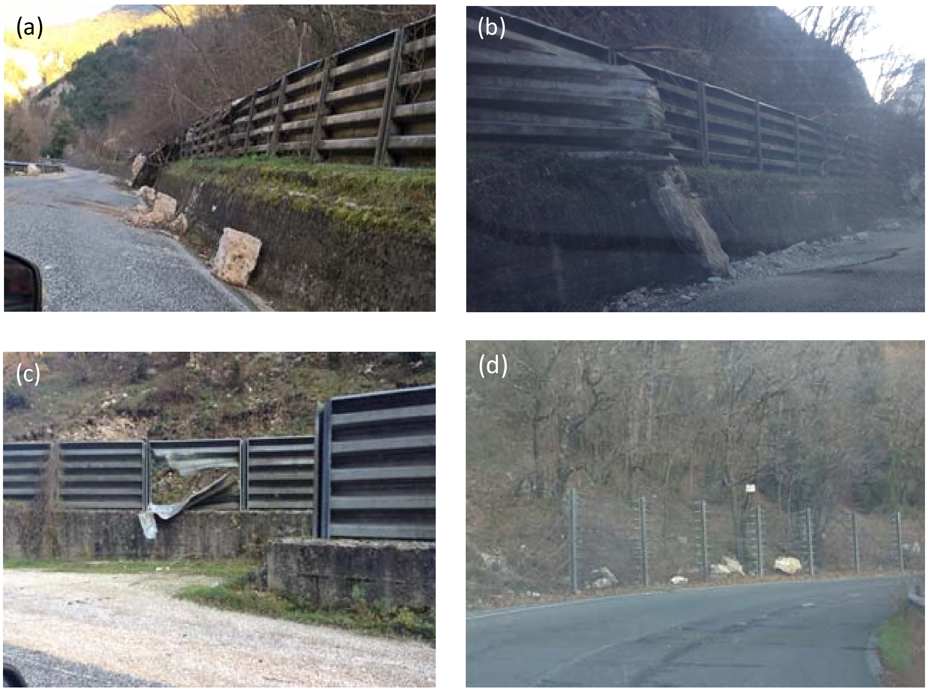

Figure 25: Slope protection damaged by boulders and rock-blocks along the regional road SP 290 in the Nera river valley (adapted from GEER, 2017).

The largest and most important rockfall occurred following the 30 October earthquake, 1 km southwest of Visso, along the steep-faced north slope of Mount Sasso Pizzuto, which is characterized by highly deformed, stratified, and fractured rocks (Maiolica Formation). The avalanche generated by this rockfall interrupted the regional road (SP 209), dammed the Nera River forming a small lake of about 2000 m^2. This feature is known as the Nera rockslide or Mount Sasso Pizzuto rock fall. This rock avalanche impacted the road transportation between Visso and the town of Terni (seat of administrative and industrial activities in the Umbria region) and the transportation network within the whole Central Apennine chain. The avalanche deposit has also damaged fish farming activities (a significant financial income for the area). The presence of such fish farming activities, along with obvious environmental concerns imposed extra care in the removal of the landslide dam, making this operation last a long time. Detailed geometric information can be found in report GEER (2017) and in Romeo et al. 2017. In both papers, for geometric characterization, for safety reasons, measurement techniques have been used without a direct approach to the landslide area. Table 2 shows that the estimated PGA value for the 30 October event at this location is 0.38 g (GEER, 2017; Zimmaro et al., 2018; Franke et al., 2018).

Quantitative measurements of the geometry of the rockslide scar and the avalanche deposit were made from photogrammetric reconstruction of images captured by UAV during flights conducted at the beginning of December, 2016 by the GEER team (GEER, 2017). A 3D reconstruction was performed using the Structure-from-Motion (SfM) computer vision post-processing and geo-referencing of the acquired UAV data (more details in GEER, 2017). The resulting 3D model is shown in Figure 26. Figure 27 shows details of the talus damming the Nera river (Franke et al., 2018). Romeo et al. (2017) have used a TruPulse™ 200 laser rangefinder. The laser sensor was placed on a tripod allowing the measure of slope distance, horizontal and vertical distance, inclination, or to calculate the elevation of any target. Thirty points were targeted on the landslide debris that covers an area of about 16,500 m^2. Furthermore, GIS analysis was defined in ArcGIS 10.1 (more details in Romeo et al. 2017).

Figure 26: Nera rockslide photographed by the GEER UAV at an elevation of 400 meters above Route SP 209. The primary rock-fall was a wedge that detached on the right side of the image and disintegrated into talus debris as it fell 330 meters to the river valley floor. The limestone bedding is visible in the scar of the wedge detachment (from GEER, 2017).

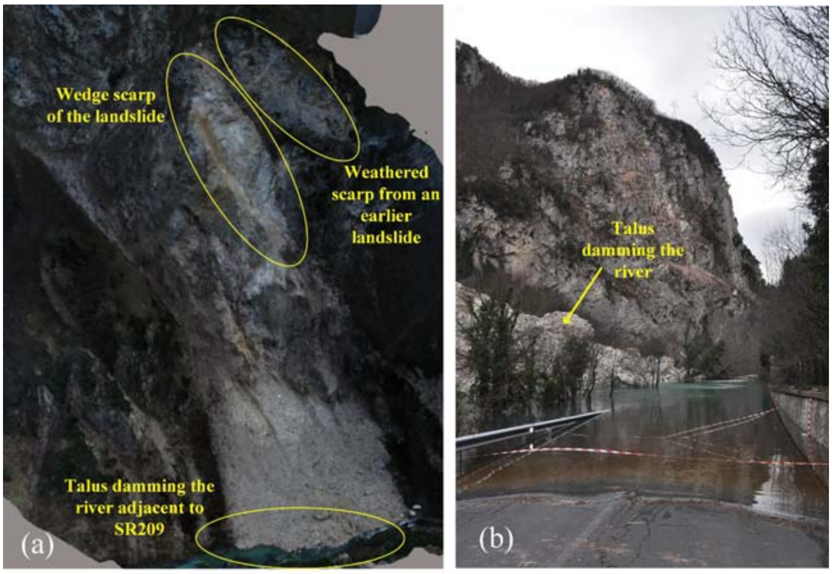

Figure 27: (a) 3D model of the Nera rockslide; (b) photograph of the dammed Nera River blocking the road (from Franke et al., 2018).

The maximum elevation difference between the rockfall source area, close to the ridge of the slope, and the SP209 road is about 300 m. The slope angle at detachment area was originally greater than 58° while after the detachment is between 75° and 80°. The rockslide scar can be approximated to those left by a rock wedge delimited by two persistent joints and the cliff surface, as can be seen in the SFM imagery of Figure 27. Bedding exhibits an apparent dip of 20°-30° towards the east and appear to be orthogonal to the joints delimiting the failed wedge, thus not playing a major role in the sliding mechanism. The apron of debris accumulation has a slope angle of about 27° and is not exactly in the perpendicular direction from the source. The accumulation area covers the foot of the slope and has an extension of about 20,000 m^2. It is difficult to estimate the percentage of the volumes of materials deriving from the source area and that from the pre-existing debris along the slope. Romeo et al. 2017 have estimated the total volume (debris originated by the rockfall plus the mobilized pre-existing talus) resulting in about 70,000 ± 8,000 m^3, of which about 50,000±60,000 m^3 deriving from the new event. This estimation is comparable to the volume of rock detached from the source area (about 40,000 m^3) determined by laser rangefinder taking into account the considerable uncertainties in evaluating the pre-existing material. Similar conclusions on pre- and post-event talus deposits have been reached by Franke et al. (2018) using UAV-based 3D models. It is not a particularly large slope failure, but probably is the biggest rockfall occurring in the area during the last two centuries.

Slope displacements in Pescara del Tronto

Significant incremental ground deformations were observed in the village of Pescara del Tronto following the 24 August event (GEER, 2016) and the October events (GEER, 2017). For safety reasons, measurement techniques have been used without a direct approach to the landslides areas after the 24 August and 30 October events. A series of UAV flights have been made to collect aerial imagery over the areas interested by landslides. UAV based photographs were subsequently processed with a SfM computer vision algorithm using Bentley ContextCapture software and Pix4D software to develop orthophotos and 3D points clouds and meshed models. Additional details about these indirect measurement techniques are provided by Franke et al. (2018).

The village suffered very heavy damage with many masonry building collapses and 48 fatalities (on 122 inhabitants) during the 24 August event and together with all downtown of Amatrice and Petrana were characterized by the highest intensity 10-11 MCS (Mercalli-Cancani-Sieberg scale; Sieberg, 1930) (Galli et al. 2016) during the sequence. A structure-by-structure damage assessment for Pescara del Tronto following the 24 August and 30 October events are discussed by Sextos et al. (2018).

Pescara del Tronto is located at the foot of the southern escarpment of Mt. Vettore, immediately downslope from the major Sibillini thrust, where the Umbro-Marchigiana carbonate sequence overlaps the turbiditic Laga formation. The town is built on a slope formed by pre-existing ancient landslide deposits consisting of angular carbonate clasts ranging in size from sands to cobbles, with interspersed pervasively fractured limestone blocks. These deposits thins proceeding towards the slope foot (the Tronto River left bank), where it overlies fluvio-lacustrine sediments including travertines. The bedrock is the Laga Formation. Few hundred of meters upslope from Pescara del Tronto, in the cataclastic carbonate rocks distributed along the thrust line, it is possible to observe a large landslide crown between elevations 900 and 1150 m a.s.l. (above sea level). Given its articulated configuration, it was likely generated by the coalescence of several complex and rotational-translational landslides whose evidence (benches, counter-slopes, and high scarps) are still present along the slope. These landslides are likely to be the source of the thick debris deposit where Pescara del Tronto is built on (Aringoli et al., 2010 and Lanzo et al., 2018).

After the August events, investigation of the 3D models of Pescara del Tronto produced by the GEER team (GEER, 2016 and 2017) revealed numerous shallow earthquake-induced landslides and retaining wall failures. The remainder of this section summarizes incremental slope instability features observed as a result of the 2016 Central Italy earthquake sequence. This analysis is largely based on multi-epoch observations mainly derived from UAV-based 3D models. A total of seven locations of interest within Pescara del Tronto have been identified to perform the cumulative damage analysis (Figure 28; GEER, 2016 and 2017).

Figure 28: 3D model of Pescara del Tronto following the 24 August event. Yellow circles highlight the seven locations of interest discussed in this report.

The largest landslide occurred on the east slope below the city (42.75057 N 13.27223 E), directly above Highway SS4 (marked as #1 in Figure 28). The landslide after the 24 August event was approximately 75m wide and 30m high. The landslide was shallow, with only the upper meter or less of soil sliding downslope. The landslide damaged retaining wall structures surrounding the city. Significant incremental movements occurred on the landslide above highway SS4 after the two October events as shown in Figures 29a-b. Limestone boulders in excess of 6 m in diameter were dislodged from the slope and rolled onto the highway.

A second, smaller shallow landslide was located above Highway SS4 (marked as #2 in Figure 28), just south of the larger landslide #1 (42.7501 N 13.2719 E). This landslide was approximately 16m wide and occurred on a slope 26m high. Figure 30 shows a comparison between 3D models produced for this feature following the 24 August and 30 October events. This smaller landslide was not observed to change significantly after the 24 August event (Figure 30a) and the 30 October earthquake (Figure 30b). In this section, the retaining wall supporting the road appeared to maintain its stability. However, significantly more structural debris from collapsed residences was observed at this location in following the 30 October earthquake.

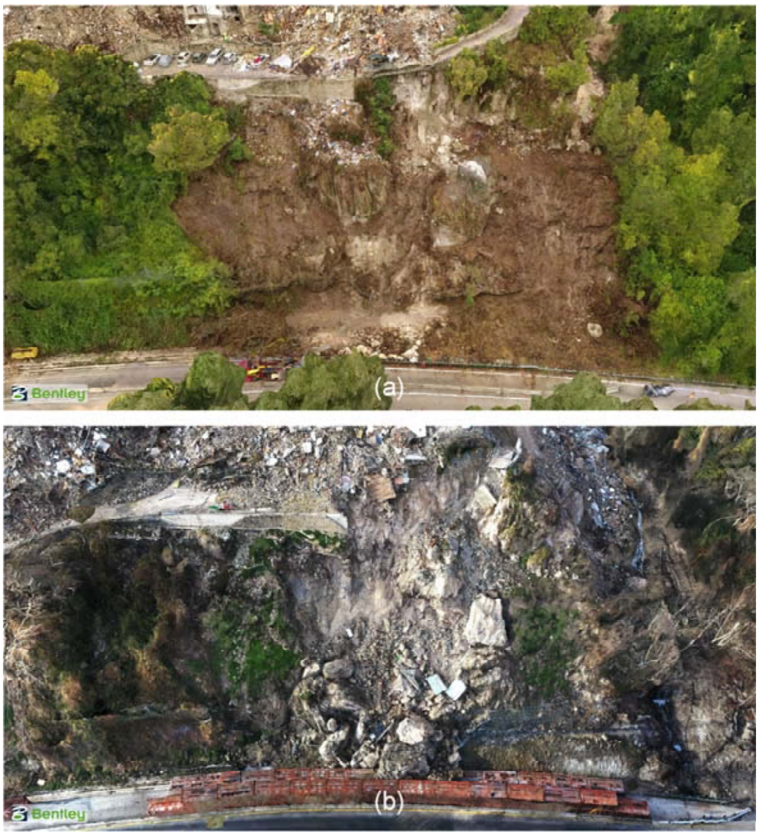

Figure 29: 3D model of landslide #1 in Pescara del Tronto following: (a) the 24 August and (b) the 30 October event (from GEER, 2017).

Figure 30: 3D model of the landslide #2 in Pescara del Tronto following: (a) the 24 August and (b) the 30 October event (from GEER, 2017).

A few of the observed slope failures in Pescara del Tronto appear to be related to potential retaining wall failures. The lower portion of Pescara del Tronto was partially supported by a 24 m-tall masonry retaining wall that surrounded the foot of the village. This wall suffered serious damage following the 24 August event (Figure 31a). Substantial damage accumulation has been observed following the October events as shown in Figure 31b. In Pescara del Tronto, structure debris was so ubiquitous that it was challenging to investigate ground deformations in this zone. Any attempt to directly investigate this zone was infeasible due to the dangerous and unstable nature of the debris field. As a result, UAV-based imagery constituted the main damage detection and analysis tool, especially after the October events. Moderate to severe damage was observed in most of the roads located adjacent to slopes and/or above retaining walls throughout Pescara del Tronto.

Figure 31: 3D model of the failed retaining wall area in Pescara del Tronto (areas #3-4 in Figure28) following: (a) the 24 August and (b) the 30 October event (from GEER, 2017).

Figure 32a shows a minor sloughing of the gulley wall observed following after the 24 August event from UAV-based imagery (feature #5 in Figure 28). In the same area, UAV-based imagery captured following the October earthquake events shown that a section of the slope nearly 9m thick and 20em wide failed into the gulley (Figure 32b). The remaining scarp is nearly 12 m in height and stands with at an angle of 52 degrees, remarkably similar to the same scarp angle that remains behind the failed lower retaining wall (i.e., Areas 3 and 4). A small residential structure that was observed to rest on top of the slope after August event had plummeted into the gulley after the October event.

Another shallow landslide occurred on the northern side of Pescara del Tronto (marked as #6 in Figure 28) following the 24 August event (Figure 33a). This landslide is approximately 17m wide by 20m high. A significant amount of structural rubble from collapsed residences is also visible in the landslide debris. Additional observed performed following the October events revealed that the depth of the landslide remained relatively unchanged, but its width expanded from 17m to more than 36m (Figure 33b). In both cases (following the 24 August and the October events) landslide size measurements have been performed using UAV-based imagery (GEER, 2017).

Figure 32: 3D model of the failure observed in area #5 in Figure 28 following: (a) the 24 August and (b) the 30 October event (from GEER, 2017).

Figure 33: 3D model of landslide #6 following: (a) the 24 August and (b) the 30 October event (from GEER, 2017).

The last landslide feature present in this report in the area of Pescara del Tronto is located on the slope bounding the gravel pit on the southern upper portion of the village adjacent to the SP 129 highway (marked as #7 in Figure 28). Observations made following the 24 August event show that the gravel pit is approximately 70m by 90m , and has 2.4V:1H side slopes comprised of slightly cemented cartaclasized limestone blocks interspersed in a gravelly-sandy matrix comprised of angular limestone clasts (Figure 34a). A dirt haul road traveling up and along the edge of the slope is located on the south side of the gravel pit. The landslide exposed about 15m of a 50 cm-diameter pipeline that was shallowly buried beneath the dirt haul road. The shape and size of the landslide remained almost unchanged following the October earthquake events as shown in Figure 34b. However, the slope beneath the haul road degraded slightly more, causing nearly half of the haul road above the landslide to disappear. Approximately 8 more meters of the pipeline became exposed from the additional slope movements, causing the pipeline to apparently sag and bow slightly. Another smaller pipe of a few centimeters' diameter was also exposed and sagging substantially along the scarp.

Figure 34: 3D model of landslide #7 and exposed pipeline following: (a) the 24 August and (b) the 30 October event (from GEER, 2017).

Slope displacements in Accumoli

Accumoli is a small village in the Rieti province, located on top of an elongated WNW-ESE ridge at an elevation spanning from 860 to 890 m a.s.l. (Figure 35). The geological bedrock in the area is the Laga Formation that therein is mainly arenaceous. This formation, which is often loosened and weathered in its shallower portions, is locally overlaid by colluvial and landslide covers. The village is located in the epicentral area of the 24 August 2016 mainshock. Accumoli suffered damages during the 14 January 1703 Valnerina earthquake (**M**6.9). Zimmaro et al. (2018) estimated PGA=0.40g during the 30 October event and PGA=0.55g during the the 24 August event in Accumoli (Table 2). Structural and landslide-related damage observed following the October events (GEER, 2017) was significantly larger than that observed following the August event and documented in GEER (2016).

Figure 35: Accumoli map with location of the landslide-related damages observed during the August and October events (from Lanzo et al., 2018).

We analyze landslide-related damage occurred in two zones: (1) Point A in Figure 35: incremental damage to a retaining wall, and (2) Point B in Figure 35, shallow slope failure on eastern side of the village. Following the 24 August event, a 4.8 m-tall retaining wall located at the eastern tip of the spur was observed to have rotated outwards 3.6 degrees, with horizontal movements of 57 cm and downward vertical movements of nearly 18 cm. A soil graben nearly 2.7 m wide was observed behind the rotated wall, with soil settlements of 45-50 cm. Much more damage was observed following the October events. It appeared that a shallow landslide developed beneath the retaining wall and caused the entire structure to slide several meters down the slope.

Figure 36 presents an aerial screenshot of the 3D model developed from UAV imagery of the site, showing evident incremental damage as a result of the earthquake sequence. The shallow landslide appeared to be limited to the upper corner of the slope, near the crown. The slide therefore likely occurred in the non-native fill slopes placed during the construction of the village. The scarp of the landslide appeared to follow the scarp of the soil graben observed behind the wall following the 24 August event, suggesting that the graben may have been caused by more than just the rotation of the retaining wall. The landslide displaced the top of the wall between 5 to 6 m horizontally and between 3 to 4 m vertically downward. In total, approximately 50 m of the retaining wall failed and slid 5 to 6 m downslope. Further south to Point A, a series of shallow cracks (orthogonal to the dip of the slope) approximately 5-14 cm in width were observed following the 24 August event. These cracks extended after the October events up to a width ranging between 80-190 cm. The depth of the cracks was approximately 55 cm.

Figure 36: 3D model screenshots following: (a) the 24 August, and (b) 30 October event (from Lanzo et al., 2018).

REFERENCES

Advanced Rapid Imaging and Analysis (ARIA) – Center for Natural Hazards, 2016. ARIA Data Share, available at https://aria-share.jpl.nasa.gov/ (last accessed 26 September 2017)

Ambraseys, N.N.: 1976, The Gemona di Friuli Earthquake of 6 May 1976, UNESCO Restricted Technical Report RP/1975-76/2.222.3, Part II.

Antonini G., Ardizzone F., Cardinali M., Galli M., Guzzetti F., Reichenbach P. (2002). Surfaces deposits and landslide inventory map of the area affected by 1997 Umbria-Marche earthquakes. Boll Soc Geol It 1, 843–853.

Aringoli D., Gentili B., Materazzi M., Pambianchi G. (2010). Mass movements in Adriatic Central Italy: activation and evolutive control factors in Landslides: Causes, types and e_ects., c 2010 Nova Science Publishers, Inc. Editors: Ernest D. Werner et al., pp. 1-71. ISBN: 978-1-60741-258-8.

Ausilio E., Zimmaro P. (2017). Landslide characterization using a multidisciplinary approach. *Measurement*, 104, 294-301.

Bird, J.F. & Bommer, J.J. (2004). Earthquake losses due to ground failure. *Engineering Geology*. vol. 75(2). pp 147-179.

Boore D.M., Stewart J. P., Seyhan E., Atkinson G.M. (2014). NGA-West 2 equations for predicting PGA, PGV, and 5%-damped PSA for shallow crustal earthquakes. *Earthquake Spectra*, 30, 1057-85.

Bozzano F., Gambino P., Prestininzi A., Scarascia Mugnozza G., Valentini G. (1998). Ground Effects Induced by the Umbria-Marche Earthquakes of September–October 1997, Central Italy, Proceedings of the 8th International Congress of the International Association for Engineering Geology and the Environment, Vancouver, Canada, 21–25 September, 1998, A.A. Balkema, Rotterdam, pp. 825–830.

Campbell K.W., Bozorgnia Y. (2014). NGA-West2 ground motion model for the average horizontal components of PGA, PGV, and 5% damped linear acceleration response spectra. *Earthquake Spectra*, 30, 1087-1115.

Carro M., De Amicis M., Luzi L., Marzorati S. (2003). The application of predictive modeling techniques to landslides induced by earthquakes: the case study of the 26 September 1997 Umbria–Marche earthquake (Italy). *Eng. Geol.* 69,139–159. DOI: 10.1016/S0013-7952(02)00277-6.

CERI working group: S. Martino, P. Caporossi, M. Della Seta, C. Esposito, A. Fantini, M. Fiorucci, R. Iannucci, G.M. Marmoni, P. Mazzanti, C. Missoni, S. Moretto, S. Rivellino, R.W. Romeo, P. Sarandrea, F. Troiani, C. Varone (2016). Sisma Centro Italia: Amatrice, Visso, Norcia Effetti-Interazione rete infrastrutturale. Available at http://www.ceri.uniroma1.it/, last accessed April 19, 2018

Chiaraluce L., Amato A., Cocco M., Chiarabba C., Selvaggi G., Di Bona M., Piccinini D., Deschamps A., Margheriti L., Courboulex F., Ripepe M. (2004). Complex Normal Faulting in the Apennines Thrust-and-Fold Belt: The 1997 Seismic Sequence in Central Italy. *Bulletin of the Seismological Society of America*, 94, 99–116.

Chiou B.S.-J., Youngs R.R. (2014). Update of the Chiou and Youngs NGA model for the average horizontal component of peak ground motion and response spectra. *Earthquake Spectra*, 30, 1117-1153.

Choi J.-K. Won J.-S., Lee S., Kim S.-W., Kim K.-D., Jung H.-S. (2011). Integration of GIS and SAR interferometry for a coal mine subsidence hazard map in Taebaek, Korea, *Int. J. Remote Sens.*, 32, 8161–8181

Cotecchia, V. and Del Prete,M.: 1984, The Reactivation of Large Flows in the Parts of Southern Italy Affected by the Earthquake of November 1980, with Reference to the Evolutive Mechanism, Proceedings of the Fourth International Symposium on Landslides, Toronto, vol. 2, pp. 33–37.

Cotecchia, V., Guerricchio, A., and Melidoro, G.: 1986, The Geomorphogenetic Crisis Triggered by the 1783 Earthquake in Calabria (Southern Italy), Proceedings of the International Symposium on Engineering Geology Problems in Seismic Areas, Bari, Italy, vol. 6, pp. 245–304.

Cruden D.M., Varnes D.J. (1996). Landslide types and processes. In: Landslides: investigation and mitigation, Turner A.K. and Shuster R.L. editors. *Transportation Research Board, Special reports*. 247, 36–75.

D'Elia, B., Esu, F., Pellegrino, A., and Pescatore, T.: 1985, Some Effects on Natural Slope Stability Induced by the 1980 Italian Earthquake, Proceedings of the Eleventh International Society of Soil Mechanics and Foundation Engineering Conference, San Francisco.

Esposito, E., Porfido, S., Simonelli, A.L., Mastrolorenzo, G., and Iaccarino, G.: 2000, Landslides and Other Surface Effects Induced by the 1997 Umbria-Marche Seismic Sequence, Engineering Geology 58, 353–376

Fielding E. J., Talebian M., Rosen P. A., Nazari H., Jackson A., Ghorashi M., Walker R. 2005. Surface ruptures and building damage of the 2003 Bam, Iran, earthquake mapped by satellite synthetic aperture radar interferometric correlation, *J. Geophys. Res.*, 110, B03302.

Franke K.W., Lingwall B.N., Zimmaro P., Kayen R.E., Tommasi P., Chiabrando F., Santo A. (2018). A Phased Reconnaissance Approach to Documenting Landslides Following the 2016 Central Italy Earthquakes. *Earthquake Spectra*. DOI: 10.1193/082117EQS165M.

Galadini F., Falcucci E., Gori S., Zimmaro P., Cheloni D., Stewart J.P. (2018). Active Faulting in Source Region of 2016-2017 Central Italy Earthquake Sequence. *Earthquake Spectra*. In Review.

Galli, P., Peronace, E., Bramerini, F., Castenetto, S., Naso, G., Cassone, F., Pallone, F. (2016). The MCS intensity distribution of the devastating 24 August 2016 earthquake in central Italy (MW 6.2). Annals of Geophysics, 59, FAST TRACK 5, 2016. DOI: 10.4401/ag-7287.

GEER (2017). Engineering Reconnaissance following the October 2016 Central Italy Earthquakes. Version 2, Zimmaro P. and Stewart J.P. editors, *GEER Association Report No. GEER-050D*. DOI: 10.18118/G6HS39.

GEER (2016). Engineering Reconnaissance of the 24 August 2016 Central Italy Earthquake. Version 2, Zimmaro P. and Stewart J.P. editors, *GEER Association Report No. GEER-050B*. DOI: 10.18118/G61S3Z.

Gigli G., Morelli S., Fornera S., Casagli N. (2014). Terrestrial laser scanner and geomechanical surveys for the rapid evaluation of rock fall susceptibility scenarios. *Landslides*, 11, 1–14. DOI: 10.1007/s10346-012-0374-0

Gori S., Falcucci E., Galadini F., Zimmaro P., Stewart J.P., Kayen R.E., Lingwall B., Moro M., Saroli M., Pizzi A., Di Domenica A. (2018). Surface faulting caused by the 2016-2017 Central Italy seismic sequence. *Earthquake Spectra*. In Review.

Govi, M.: 1977b, Photo-interpretation and Mapping of the Landslides Triggered by the Friuli Earthquake (1976), International Association of Engineering Geology Bulletin 15, 67–72.

Gregor N., Silva W., Darragh R. (2002). Development of attenuation relations for peak particle velocity and displacement. *A PEARL report to PG&E/CEC/Caltrans*, June 12, 2002.

Gruppo di Lavoro INGV sul terremoto di Amatrice, INGV (2016). Secondo rapporto di sintesi sul Terremoto di Amatrice Ml 6.0 del 24 Agosto 2016 (Italia Centrale). DOI: 10.5281/zenodo.154400.

Gruppo di Lavoro ISPRA (2016). *Report attività svolta da ISPRA in data 25-26/08/2016*. Centro per la micro zonazione sismica e le sue applicazioni.

Hungr O., Leroueil S., Picarelli L. (2014). The Varnes classification of landslide types, an update. *Landslides*, 11, 167-194.

Jayaram N., Baker J.W. (2009). Correlation model for spatially distributed ground-motion intensities, *Earthquake Engineering and Structural Dynamics*, 38, 1687–1708.

Jo M.-J., Won J.-S., Kim S.-W., Jung H.-S. (2010). A time-series SAR observation of surface deformation at the southern end of the San Andreas fault zone. *Geosci. J.*, 14, 277-287.

Jung H.-S., Lu Z., Won J.S., Poland M.P., Miklius A. (2011). Mapping three-dimensional surface deformation by combining multiple-aperture interferometry and conventional interferometry: Application to the June 2007 eruption of Kilauea volcano, Hawaii. *IEEE Geosci. Remote Sens. Lett.*, 8, 34-38.

Keefer D.K. (1984). Landslides caused by earthquakes. *Geol Soc Am Bull*, 95, 406–421

Keefer D.K. (1985). Landslides caused by earthquakes: Reply. *Geol Soc Am Bull*, 96, 1093-1094

Keefer D.K. (2002). Investigating landslides caused by earthquakes – A historical Review, Surv. Geohys., 23, 473–510.

Lanzo G., Tommasi P., Ausilio E., Aversa S., Bozzoni F., Cairo R., d'Onofrio A., Durante M.G., Foti S., Giallini S., Mucciacciaro M., Pagliaroli A., Sica S., Silvestri F., Vessia G., Zimmaro P. (2018).

Reconnaissance of geotechnical aspects of the 2016 Central Italy earthquakes. *Bulletin of Earthquake Engineering*. DOI: 10.1007/s10518-018-0350-8.

Lee W., Lu Z., Won J.-S., Jung H.-S., Dzurisin D. (2013). Dynamic deformation of Seguam Island, Alaska, 1992–2008, from multi-interferogram InSAR processing. *J. Volcanol. Geotherm. Res.*, 260, 43-51.

Pavlides, S., Chatzipetros, A., Papathanasiou, G., Georgiadis, G., Sboras, S., Valkaniotis, S. (2017). Ground deformation and fault modeling of the 2016 sequence (24 Aug.–30 Oct.) in central Apennines (Central Italy). *Bulletin of the Geological Society of Greece,* 51, 76-112.

Piatanesi A., Cirella A. (2009). Rupture Process of the 2009 Mw6.3 L'Aquila (Central Italy) Earthquake from Nonlinear Inversion of Strong Motion and GPS Data. *Istituto Nazionale di Geofisica e Vulcanologia (INGV),* Rome, Italy.

Polcari, M., Montuori, A., Bignami, C., Moro, M., Stramondo, S., Tolomei, C. (2017). Using multi-band InSAR data for detecting local deformation phenomena induced by the 2016–2017 Central Italy seismic sequence. *Remote Sensing of Environment*, 201, 234-242.

Rathje E.M., Carr L.P. (2010). Satellite Observations of Landslides Caused by the 2008 Wenchuan Earthquake in China. In *Proceedings, 9th US National and 10th Canadian Conference on Earthquake Engineering: Reaching Beyond Borders*, July 2010, Toronto, Canada.

Rathje E.M., Franke K.W. (2016). Remote sensing for geotechnical earthquake reconnaissance. *Soil Dynamics and Earthquake Engineering*, 91, 304-316.

Rodríguez C.E., Bommer J.J., Chandler R.J. (1999). Earthquake-induced landslides: 1980-1997. *Soil Dynamics and Earthquake Engineering*, 18, 325–346

Romeo, S., Di Matteo, L., Melelli, L., Cencetti, C., Dragoni, W., Fredduzzi, A. (2017). Seismic-induced rockfalls and landslide dam following the October 30, 2016 earthquake in Central Italy. *Landslides*, 14, 1457-1465.

Sarconi M. (1784). Osservazioni Fatte Nelle Calabrie e Nella Frontiera di Valdemone sui Fenomeni del Tramoto del 1783 e Sulla Geografia Fisica di Quelle Regioni, Reali Accademia delle Scienze e Belle Lettere. Napoli.

Sextos A., De Risi R., Pagliaroli A., Foti S., Passeri F., Ausilio E., Cairo R., Capatti M.C., Chiabrando F., Chiaradonna A., Dashti S., De Silva F., Dezi F., Durante M.G., Giallini S., Lanzo G., Sica S. Simonelli A.L., Zimmaro P. (2018). Local site effects and incremental damage of buildings during the 2016 Central Italy earthquake sequence. *Earthquake Spectra*. DOI: 10.1193/100317EQS194M.

Sieberg A. (1930). Geologie der Erdbeben. Handboch der Geophysic, 2, 4, 552-554 [Tabb. 100, 101, 102, 103], Berlin.

Stewart J.P., Lanzo G., Pagliaroli A., Scasserra G., Di Capua G., Peppoloni S., Darragh R., Gregor N. (2012). Ground Motion Recordings from the Mw 6.3 2009 L'Aquila Earthquake in Italy and their Engineering Implications. *Earthquake Spectra*, 28, 317-345.

Yun S.-H., Fielding E.J., Simons M., Rosen P., Owen S., Webb F. (2011). Damage proxy map of M 6.3 Christchurch earthquake using InSAR coherence. Fringe Workshop, *Advances in the science and applications of SAR interferometry from ESA and 3rd party missions*. Frascati, Italy, https://earth.esa.int/documents/10174/1567329/Yun_FRINGE2011.pdf.

Yun S.-H., Hudnut K., Owen S., Webb F., Simons M., Sacco P., Gurrola E., Manipon G., Liang C., Fielding E.J., Milillo P., Hua H., Coletta A. (2015). Rapid Damage Mapping for the 2015 Mw 7.8 Gorkha Earthquake Using Synthetic Aperture Radar Data from COSMO–SkyMed and ALOS-2 Satellites. *Seismological Research Letters*, 86, 1549-1556.

Zhang L., Lu Z., Ding X., Jung H.-S., Feng G., Lee C.-W. (2012). Mapping ground surface deformation using temporarily coherent point SAR interferometry: Application to Los Angeles Basin. *Remote Sens. Environ.*, 117, 429-439.

Zimmaro P., Scasserra G., Stewart J.P., Kishida T., Tropeano G., Castiglia M., Pelekis P. (2018). Strong Ground Motion Characteristics from 2016 Central Italy Earthquake Sequence. *Earthquake Spectra*. DOI: 10.1193/091817EQS184M.

Zimmaro P., Stewart J.P. (2017). Site-specific seismic hazard analysis for Calabrian dam site using regionally customized seismic source and ground motion models. *Soil Dynamics and Earthquake Engineering*, 94, 179-192.